Ultramicroscopy 277 (2025) 114218

Contents lists available at ScienceDirect

Ultramicroscopy

journal homepage: www.elsevier.com/locate/ultramic

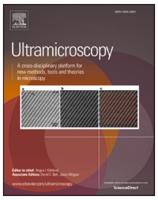

# Quantitative comparison of long-range electric field measurements using off-axis electron holography and 4D-STEM *via* differential phase contrast

Janghyun Jo [a,*], Ivan Lazić [b], Eric G.T. Bosch [b], Stefano Vespucci [b], Giulio Pozzi [a,c], Rafal E. Dunin-Borkowski [a]

[a] *Ernst Ruska-Centre for Microscopy and Spectroscopy with Electrons, Forschungszentrum Jülich, Jülich 52425, Germany*
[b] *Thermo Fisher Scientific, Materials and Structural Analysis, Achtseweg Noord 5, Eindhoven 5651GG, the Netherlands*
[c] *Department FIM, University of Modena and Reggio Emilia, via G. Campi 213/a, Modena 41125, Italy*

ARTICLE INFO

*Keywords:*
Transmission electron microscopy
Long-range electric field
Off-axis electron holography
Perturbed reference wave
4D-STEM
Differential phase contrast

ABSTRACT

Phase contrast techniques in the transmission electron microscope (TEM), such as off-axis electron holography (OAEH) and four-dimensional scanning TEM (4D-STEM), are widely utilized for mapping electromagnetic fields both within and surrounding nanoscale materials. In this study, the two techniques are used to measure long-range electrostatic potentials and electric fields generated by electrically-biased colinear conducting needles. The results are compared between the two techniques and with a theoretical model. The experimental measurements obtained using OAEH and 4D-STEM *via* differential phase contrast reveal discrepancies in the magnitudes and distributions of the electric fields surrounding the needles. A comparison of both approaches with a theoretical model reveals that the discrepancy results from perturbation of the reference wave in OAEH by the highly extended electric field outside the needles, leading to an underestimate of the electrostatic potential when using OAEH. In contrast, the 4D-STEM measurements are more directly interpretable. We provide a theoretical background for the OAEH results, which fully explains and supports the findings.

## 1. Introduction

Quantitative measurements of electromagnetic fields are of great interest for fundamental research and for the development of next-generation electronic and spintronic devices. For example, a knowledge of the electric field around a field emitter tip plays an important role in understanding its field emission properties, including the current density and emission area, as well as the spatial and temporal coherence, which are related to the size of the tip and the energy spread of the electron beam, respectively [1–3]. Similarly, the details of the electric field are essential to understand both the field evaporation process from a needle-shaped specimen and the trajectory of the ions to the detector during atom probe tomography and therefore to improve the fidelity of the reconstruction of the three-dimensional atomic positions in the sample [4]. In a further example, a knowledge of the internal and stray fields of electronic and spintronic devices is important to understand their operating principles and failure mechanisms [5–7].

Different transmission electron microscopy (TEM) techniques [8,9] can be used to obtain electron optical phase information about a sample, in order to visualize the electromagnetic fields within and around it. For a non-magnetic sample, the fields are purely electrostatic. An electrostatic (vector) field can equivalently be represented by the gradient of the corresponding (scalar) electrostatic potential. Here, we consider two TEM techniques: electron holography and four-dimensional scanning TEM (4D-STEM), which usually involve the use of parallel and scanned convergent illumination, respectively. There are many different modes of each technique. For electron holography, they include in-line and off-axis electron holography [10–17]. For 4D-STEM, they include (annular) bright-field ((A)BF) and annular dark-field (ADF) approaches [8,9,18,19], as well as differential phase contrast (DPC) STEM [8,20–26] and electron ptychography [27–30].

For electron holography, we focus on the TEM mode of off-axis electron holography (OAEH), which allows for quantitative analysis based on rigorous theory [12]. OAEH is a well-established TEM technique for measuring potentials and fields within and outside materials with nanometre or atomic spatial resolution [10,11,26]. An electrostatic biprism, which is typically located below the specimen, is used to bend two parts of the electron wave in order to overlap their wavefronts in the

---

* Corresponding author.
*E-mail address:* j.jo@fz-juelich.de (J. Jo).

https://doi.org/10.1016/j.ultramic.2025.114218
Received 12 March 2025; Received in revised form 15 July 2025; Accepted 18 July 2025

image plane to produce an electron hologram. The hologram is used to record an interference pattern formed by an object wave passing through the specimen and a reference wave passing through an adjacent region of vacuum. The amplitude and phase of the exit electron wave from the sample can be retrieved from the hologram. For a thin, weakly diffracting sample, the phase records the projected electrostatic potential (scalar). The gradient (differential) of the phase can then be calculated numerically to determine the components of the projected in-plane electric field (vector).

For 4D-STEM, we focus on DPC-STEM [20–26]. DPC-STEM has been used to directly measure the gradient (differential) of the phase by measuring the deflection of a convergent electron beam with respect to its direction when the sample is absent. This deflection directly represents the in-plane component of the projected electric field (vector) and is captured conveniently in the far field or, equivalently, in the diffraction plane of the projection lens of the TEM column [24,25], where a convergent beam electron diffraction (CBED) pattern is formed. The CBED pattern can be recorded fully and its centre of mass (COM) computed digitally or, more conventionally, a segmented detector can be used [20,21,24–26], for example by subtracting signals recorded from opposite segments when a four-quadrant detector is used. With the recent development of fast pixelated detectors, 4D-STEM has been widely adopted for measuring electromagnetic fields [31–33]. The ability to record full CBED patterns enables techniques that make use of their details and broad range of spatial frequencies [34,35], such as ptychography [27,30], to be used to extract the phase of the sample transmission function. The phase can also be obtained by integration (*i.e.*, calculation of the inverse gradient) of a measured DPC-STEM dataset. This approach is referred to as integrated differential phase contrast STEM (iDPC-STEM) [24,25,33]. When a camera is used so that the COM of a full CBED pattern is computed, then (i)DPC-STEM can be referred to as (i)COM-STEM [24,25,33].

In the present work, we report a quantitative comparison of long-range electrostatic field and potential measurements recorded from the same specimen using OAEH and 4D-STEM in DPC-STEM mode (making use of a camera to compute the COM directly). Both techniques are used to measure the projected electrostatic potential and projected in-plane electric field in vacuum around electrically-biased colinear conducting needles. Differences between the results obtained using the two techniques are investigated thoroughly. A comparison of the measurements with a theoretical model based on analytical expressions for the electrostatic potential and electric field of a line charge is used to establish that a perturbed reference wave (PRW) effect in OAEH is primarily responsible for the discrepancy between the techniques. The analysis makes use of a model-based iterative reconstruction algorithm (MBIR) to determine the charge distribution in the needle-shaped sample. The study of fields and potentials in vacuum allows the effects of dynamical diffraction in the specimen to be avoided. The results illustrate both the advantages of using electron holography and 4D-STEM when measuring long-range electric fields and the need to compare results obtained using complementary techniques to understand whether artefacts are present in such measurements.

## 2. Experimental details

Two Au needles were prepared by electrochemical etching Au wires of length ~1 cm and diameter 25 μm in an electrochemical etching machine (ElectroPointer, Simplex Scientific). A DC voltage of 4 V was used to apply an electric current through each wire in an electrolyte solution comprising a 50:50 mixture of 30 % HCl and ethanol. The two Au wires, whose tips had been etched to have diameters of below 100 nm, were loaded into a Nanofactory STM-TEM specimen holder such that they were separated by a distance of ~200 nm, as shown in Fig. 1(a). A bias of +50 V was applied to the lower needle, while the upper needle was grounded (Fig. 1(b)).

4D-STEM data were recorded on an FEI Titan G2 80–200 ChemiSTEM equipped with a Schottky-type high brightness electron gun and a probe Cs corrector (CEOS DCOR) [36]. The microscope was aligned in nanobeam diffraction mode with a convergence semi-angle (CSA) of 3.5 mrad. The electron beam was scanned across the needles with a dwell time of 1 ms and CBED patterns were recorded using an Electron Microscope Pixel Array Detector (EMPAD), as shown in Fig.1(c). A camera length of 3.5 m was used to maximize the beam deflection, in order to achieve high sensitivity for measuring shifts of the CBED patterns. The

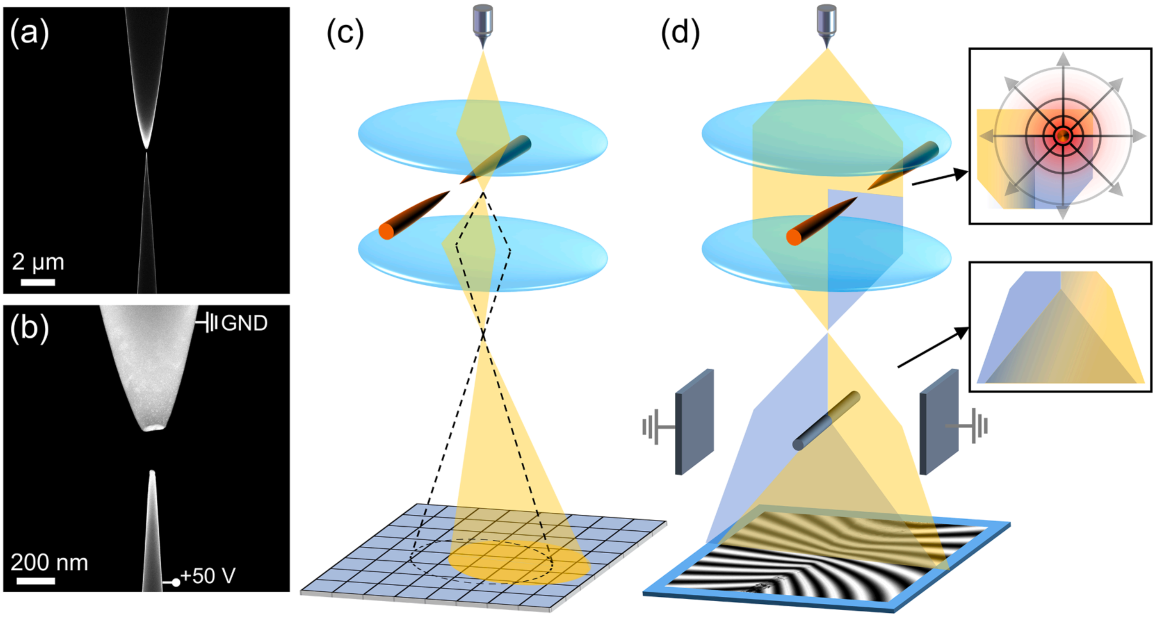

**Fig. 1.** Experimental setup for 4D-STEM and OAEH measurements of electrically-biased colinear Au needles. (a) ADF-STEM image of two Au needles facing each other in a TEM specimen holder. (b) Magnified image of the tips of the needles, which have a head-to-head separation of 200 nm. (c) Schematic diagram of the 4D-STEM configuration, with a convergent electron beam scanning across the two needles. The CBED patterns are recorded in the back focal plane, which is equivalent to the far field. (d) Schematic diagram of the OAEH configuration, with a parallel electron beam illuminating the two needles. A biprism is located in the projection system. The hologram is recorded in the image plane.

diameter of the full bright field disk (49 pixels) was slightly larger than 1/3 of the size of the detection area of the EMPAD (128 pixels). In order to extract only the projected electrostatic potential and electric field and to eliminate the effects of the stray field of the needles, reference 4D-STEM data were recorded by scanning the electron beam across the needles with a bias voltage of 0 V. The COM positions from the reference data were subtracted from data recorded with a voltage applied between the needles.

OAEH was performed on an FEI Titan G2 60–300 TEM equipped with a Schottky-type high brightness electron gun, an image Cs corrector and two electron biprisms [37]. Electron holograms were recorded at an accelerating voltage of 300 kV in Lorentz mode with a large field of view (FOV) using a Gatan K2-IS direct electron detection camera (Fig. 1(d)). The biprism voltage was varied between 70 and 280 V. Electron holograms were recorded using an acquisition time of 8 s with a fringe contrast in vacuum of 45 % for a biprism voltage of 140 V. Vacuum reference holograms were recorded for 8 s from a vacuum region and used to remove distortions associated with the imaging and recording systems of the microscope. The beam intensity was adjusted so that a dose rate of 10 electrons per pixel per second (eps) could be achieved using the K2 camera. In order to eliminate the contribution to the recorded phase shift from the mean inner potential of the needles, phase images recorded with different bias voltages applied to the needle (*e.g.*, one at +50 V and the other at 0 V) were subtracted from each other. For reconstruction, each hologram recorded with a bias voltage of +50 V was shifted manually to align it with respect to the corresponding hologram recorded with a bias voltage of 0 V, as the positions of the needles moved across the detector due to deflection of the electron beam by the applied voltage. The two resulting complex images were divided to obtain the amplitude ratio and the phase difference between them.

For each experiment, the magnification was adjusted so that the FOV was ~1.5 µm. The positions of the needles were kept unchanged in the specimen holder during transfer and measurements on both microscopes.

## 3. Theoretical basis

### 3.1. *OAEH: theory of electrostatic potential and electric field measurement*

For OAEH, the imaging procedure can be divided into two steps: hologram acquisition and amplitude and phase recovery [10,11,26]. The electron wave function in the detector plane $\psi_D^O(\boldsymbol{r})$ is, in this

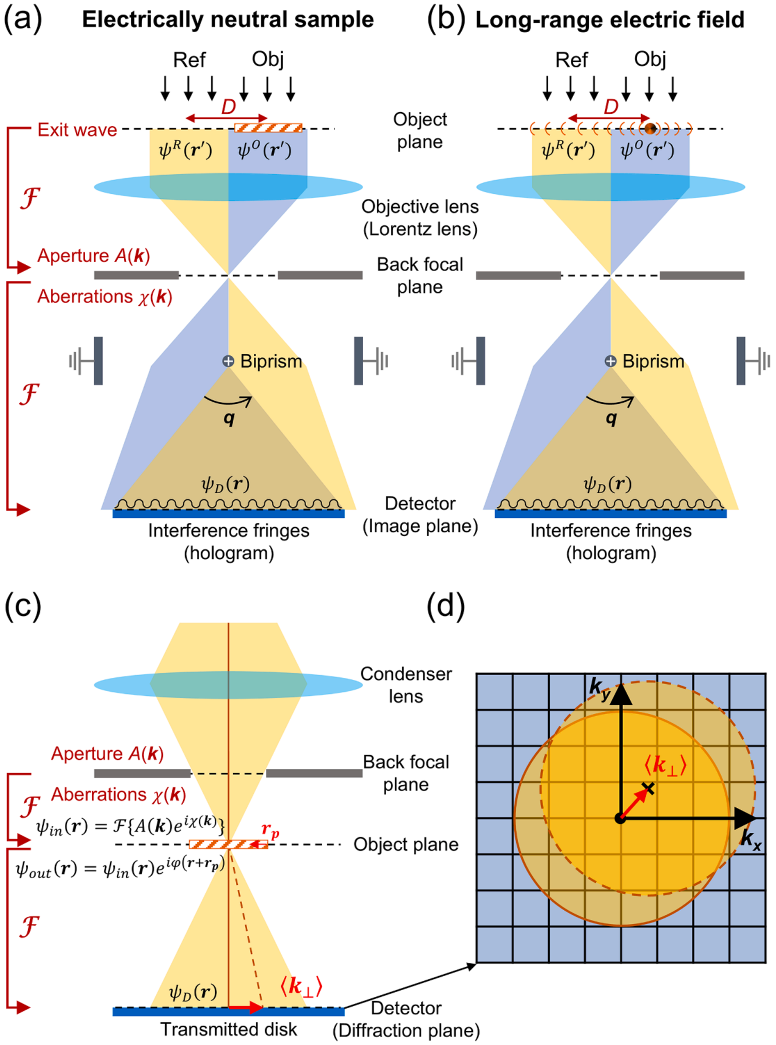

**Fig. 2.** Schematic illustrations of the underlying theories of OAEH and 4D-STEM. The optical paths are not to scale. (a, b) TEM configuration for OAEH. Two consecutive FTs take the exit wave from the sample and the reference wave, first to the back focal plane of the objective lens and then to the image plane. (c, d) 4D-STEM configuration. A first FT forms a convergent probe, while a second FT takes the exit wave of the sample to the far field. In (a), the sample is electrically neutral. In (b), there is a long-range electric field outside the sample. (c) Electron optical setup for 4D-STEM *via* DPC. (d) Recording of a CBED pattern on a pixelated detector, from which the COM shift vector is computed for DPC.

configuration, the electron wave function in the image plane of the objective lens (Figs. 2(a) and (b)). The lens acts to Fourier transform (FT) the exit wave function of the sample $\psi^O(\boldsymbol{r})$ from the object plane to the back focal plane. Here, it is cut off by a lens aperture $A(\boldsymbol{k})$ and modified by aberrations $\chi(\boldsymbol{k})$, yielding $\psi^O_{BFP}(\boldsymbol{k}) = \mathscr{F}\{\psi^O(\boldsymbol{r})\}(\boldsymbol{k})A(\boldsymbol{k})e^{-i\chi(\boldsymbol{k})}$, where the operator $\mathscr{F}$ represents a FT, which is defined as $\mathscr{F}\{f(\boldsymbol{r})\}(\boldsymbol{k}) = \int\int_{-\infty}^{\infty} f(\boldsymbol{r})e^{-2\pi i\boldsymbol{k}\cdot\boldsymbol{r}}d^2\boldsymbol{r}$ and its inverse as $\mathscr{F}^{-1}\{f(\boldsymbol{k})\}(\boldsymbol{r}) = \int\int_{-\infty}^{\infty} f(\boldsymbol{k})e^{2\pi i\boldsymbol{k}\cdot\boldsymbol{r}}d^2\boldsymbol{k}$ If the biprism is switched off, then another FT brings the electron wave function from the back focal plane to the image plane, as illustrated in Fig. 2(a), yielding $\psi^O_D(\boldsymbol{r}) = \mathscr{F}\{\psi^O_{BFP}(\boldsymbol{k})\}(\boldsymbol{r})$. In this paper, we follow the convention in Ref. [38], which describes the process of image formation in terms of two direct Fourier transforms. The object wave function at the detector $\psi^O_D(\boldsymbol{r})$ can be expressed in the form

$$\begin{aligned}\psi^O_D(\boldsymbol{r}) &= \mathscr{F}\left\{\mathscr{F}\left\{\psi^O(\boldsymbol{r})\right\}(\boldsymbol{k})\cdot A(\boldsymbol{k})e^{-i\chi(\boldsymbol{k})}\right\}(\boldsymbol{r})\\ &= \left(\psi^O(-\boldsymbol{r}') * \mathscr{F}\left\{A(\boldsymbol{k})e^{-i\chi(\boldsymbol{k})}\right\}(\boldsymbol{r}')\right)(\boldsymbol{r}),\end{aligned} \tag{1}$$

where $\boldsymbol{r} = (x, y)$ and $\boldsymbol{k} = (k_x, k_y)$ are two-dimensional vectors in the object (and image) and back focal planes, respectively, the symbol $*$ refers to convolution and the FT property $\mathscr{F}\{\mathscr{F}\{f(\boldsymbol{r})\}(\boldsymbol{k})\}(\boldsymbol{r}) = f(-\boldsymbol{r})$ has been applied. For convenience, by ignoring the magnification factor [38], the final electron wave function expressions for the object and reference waves at the detector plane take the forms

$$\psi^O_D(\boldsymbol{r}) = \left(\left(A_0(-\boldsymbol{r}')e^{i\varphi(-\boldsymbol{r}')}\right) * \mathscr{F}\left\{A(\boldsymbol{k})e^{-i\chi(\boldsymbol{k})}\right\}(\boldsymbol{r}')\right)(\boldsymbol{r}) \tag{2a}$$

$$\psi^R_D(\boldsymbol{r}) = \left(1 * \mathscr{F}\left\{A(\boldsymbol{k})e^{-i\chi(\boldsymbol{k})}\right\}(\boldsymbol{r}')\right)(\boldsymbol{r}), \tag{2b}$$

where $A_0(\boldsymbol{r})$ and $\varphi(\boldsymbol{r})$ are the amplitude and phase of the sample exit wave function $\psi^O(\boldsymbol{r}) = A_0(\boldsymbol{r})e^{i\varphi(\boldsymbol{r})}$ (Eq. (2a)) and 1 denotes the reference plane wave function $\psi^R(\boldsymbol{r})$ that passes through vacuum (Eq. (2b)), respectively, as shown in Fig. 2(a). Since the reference wave is assumed to be an ideal plane wave here, an interference distance $D$ between the object and reference waves does not need to be included in Eq. (2b). It should be noted that the reference wave and object wave have switched places at the detector plane, as the lens introduces an inversion.

For an ideal lens with no aberrations (*i.e.*, $\chi(\boldsymbol{k}) = 0$) and an infinitely large aperture (*i.e.*, $A(\boldsymbol{k}) = 1$), $\mathscr{F}\{A(\boldsymbol{k})e^{-i\chi(\boldsymbol{k})}\}(\boldsymbol{r}') = \mathscr{F}\{1\}(\boldsymbol{r}') = \delta(\boldsymbol{r}')$ and Eq. (2) simplifies to

$$\psi^O_D(\boldsymbol{r}) = \left(\psi^O(-\boldsymbol{r}') * \delta(\boldsymbol{r}')\right)(\boldsymbol{r}) = \psi^O(-\boldsymbol{r}) = A_0(-\boldsymbol{r})e^{i\varphi(-\boldsymbol{r})} \tag{3a}$$

$$\psi^R_D(\boldsymbol{r}) = \left(\psi^R(-\boldsymbol{r}') * \delta(\boldsymbol{r}')\right)(\boldsymbol{r}) = \psi^R(-\boldsymbol{r}) = 1. \tag{3b}$$

The image of the object intensity $I(\boldsymbol{r}) = |\psi^O_D(\boldsymbol{r})|^2 = \psi^O_D(\boldsymbol{r})\overline{\psi^O_D(\boldsymbol{r})} = |A_0(-\boldsymbol{r})|^2$ measured on the detector is just the amplitude of the sample exit wave squared, which carries little or no information for a thin sample, while the phase is lost. This is the well-known phase problem.

In contrast, when the biprism is switched on, the two parts of the electron wave are tilted towards each other by deflection vectors $\frac{\boldsymbol{q}}{2}$ and $-\frac{\boldsymbol{q}}{2}$, causing them to interfere to form a new wave function $\psi_D(\boldsymbol{r})$ in the detector plane, which is a mixture of the object and reference waves, in the form

$$\psi_D(\boldsymbol{r}) = \psi^O_D(\boldsymbol{r})e^{2\pi i\frac{\boldsymbol{q}}{2}\cdot\boldsymbol{r}} + \psi^R_D(\boldsymbol{r})e^{-2\pi i\frac{\boldsymbol{q}}{2}\cdot\boldsymbol{r}}. \tag{4}$$

The intensity of the final wave function $I(\boldsymbol{r})$ is the modulus squared of $\psi_D(\boldsymbol{r})$ and is referred to as a hologram. It takes the general form

$$\begin{aligned}I(\boldsymbol{r}) &= \psi_D(\boldsymbol{r})\overline{\psi_D(\boldsymbol{r})}\\ &= \left|\psi^R_D(\boldsymbol{r})\right|^2 + \left|\psi^O_D(\boldsymbol{r})\right|^2 + \psi^O_D(\boldsymbol{r})\overline{\psi^R_D(\boldsymbol{r})}e^{2\pi i\boldsymbol{q}\cdot\boldsymbol{r}} + \overline{\psi^O_D(\boldsymbol{r})}\psi^R_D(\boldsymbol{r})e^{-2\pi i\boldsymbol{q}\cdot\boldsymbol{r}}\end{aligned} \tag{5}$$

where the tilts of the object and reference waves by the biprism are specified by two-dimensional reciprocal space vectors $\frac{\boldsymbol{q}}{2}$ and $-\frac{\boldsymbol{q}}{2}$. For an ideal lens, by making use of Eq. (3), this expression simplifies to

$$I(\boldsymbol{r}) = \psi_D(\boldsymbol{r})\overline{\psi_D(\boldsymbol{r})} = 1 + {A_0}^2(-\boldsymbol{r}) + 2A_0(-\boldsymbol{r})cos(2\pi\boldsymbol{q}\cdot\boldsymbol{r} + \varphi(-\boldsymbol{r})), \tag{6}$$

which now carries information about both the amplitude and the phase of the sample exit electron wave $\psi^O(\boldsymbol{r}) = A_0(\boldsymbol{r})e^{i\varphi(\boldsymbol{r})}$, unlike the intensity of the wave function given by Eq. (3).

Recovery of the amplitude $A_0(\boldsymbol{r})$ and phase $\varphi(\boldsymbol{r})$ of the exit electron wave function $\psi^O(\boldsymbol{r})$ from the hologram $I(\boldsymbol{r})$ can be described by starting from the general expression in Eq. (5). An inverse Fourier transform (IFT) of Eq. (5) yields the elegant expression

$$\begin{aligned}&\mathscr{F}^{-1}\{I(\boldsymbol{r})\}(\boldsymbol{k}) = \mathscr{F}^{-1}\left\{\left|\psi^R_D(\boldsymbol{r})\right|^2\right\}(\boldsymbol{k}) + \mathscr{F}^{-1}\left\{\left|\psi^O_D(\boldsymbol{r})\right|^2\right\}(\boldsymbol{k})\\ &+ \mathscr{F}^{-1}\left\{\psi^O_D(\boldsymbol{r})\overline{\psi^R_D(\boldsymbol{r})}\right\}(\boldsymbol{k}+\boldsymbol{q}) + \mathscr{F}^{-1}\left\{\overline{\psi^O_D(\boldsymbol{r})}\psi^R_D\right\}(\boldsymbol{k}-\boldsymbol{q}),\end{aligned} \tag{7}$$

where the FT shift property $\mathscr{F}\{f(\boldsymbol{r})e^{2\pi i\boldsymbol{q}\cdot}\ \boldsymbol{r}\}(\boldsymbol{k}) = \mathscr{F}\{f(\boldsymbol{r})\}(\boldsymbol{k}-\boldsymbol{q})$ has been used. By making use of the property of convolution that $(1 * \mathscr{F}\{f(\boldsymbol{k})\}(\boldsymbol{r}'))(\boldsymbol{r}) = f(0)$, the reference wave (Eq. (2b)) becomes $\psi^R_D(\boldsymbol{r}) = (1 * \mathscr{F}\{A(\boldsymbol{k})e^{-i\chi(\boldsymbol{k})}\}(\boldsymbol{r}'))(\boldsymbol{r}) = A(0)e^{-i\chi(0)} = 1$, as the aperture is transparent at the origin ($A(0) = 1$), while the aberration function is not included, as $\chi(0) = 0$. When combined with Eq. (7), the final expression becomes

$$\begin{aligned}\mathscr{F}^{-1}\{I(\boldsymbol{r})\}(\boldsymbol{k}) \quad = \quad & \delta(\boldsymbol{k}) + \mathscr{F}^{-1}\left\{\left|\psi^O_D(\boldsymbol{r})\right|^2\right\}(\boldsymbol{k}) + \mathscr{F}^{-1}\left\{\psi^O_D(\boldsymbol{r})\right\}(\boldsymbol{k}+\boldsymbol{q})\\ & + \mathscr{F}^{-1}\left\{\overline{\psi^O_D(\boldsymbol{r})}\right\}(\boldsymbol{k}-\boldsymbol{q}).\end{aligned} \tag{8}$$

The first two terms in Eq. (8) are IFTs of a reference plane wave and a bright-field image of the specimen $I^{TEM}(\boldsymbol{r}) = |\psi^O_D(-\boldsymbol{r})|^2$ centered at the origin of reciprocal space, respectively. The last two terms are the IFT of the object wave function at the detector centered at $\boldsymbol{k} = -\boldsymbol{q}$ and the IFT of the complex conjugate of the object wave function at the detector centered at $\boldsymbol{k} = \boldsymbol{q}$, corresponding to two sidebands (SBs) in reciprocal space. The reason for starting with an IFT rather than a FT in Eq. (7) becomes clear in the next step. Combining the object wave function at the detector $\psi^O_D(\boldsymbol{r})$ given by Eq. (1) with Eq. (8) yields the expression

$$\begin{aligned}&\mathscr{F}^{-1}\{I(\boldsymbol{r})\}(\boldsymbol{k}) = \delta(\boldsymbol{k}) + \mathscr{F}\left\{I^{TEM}(\boldsymbol{r})\right\}(\boldsymbol{k})\\ &+\mathscr{F}\left\{\psi^O(\boldsymbol{r})\right\}(\boldsymbol{k}+\boldsymbol{q})\cdot A(\boldsymbol{k}+\boldsymbol{q})e^{-i\chi(\boldsymbol{k}+\boldsymbol{q})}\\ &+\mathscr{F}\left\{\overline{\psi^O(\boldsymbol{r})}\right\}(\boldsymbol{k}-\boldsymbol{q})\cdot A(\boldsymbol{k}-\boldsymbol{q})e^{-i\chi(\boldsymbol{k}-\boldsymbol{q})},\end{aligned} \tag{9}$$

where the convolution theorem in the third and fourth terms and $\mathscr{F}^{-1}\ \{f(-\boldsymbol{r})\}(\boldsymbol{k}) = \mathscr{F}\{f(\boldsymbol{r})\}(\boldsymbol{k})$ have been applied and inversion of the object has been eliminated. The second term in Eq. (9) is a FT of a regular TEM image. In the weak phase object approximation ($\varphi(\boldsymbol{r}) \ll 1$), $\mathscr{F}\{I^{TEM}(\boldsymbol{r})\}(\boldsymbol{k}) \approx 2A(\boldsymbol{k})e^{i\chi_{odd}(\boldsymbol{k})}(\cos\chi_{ev}(\boldsymbol{k})\cdot$ $\mathscr{F}\{A_0(\boldsymbol{r})\}(\boldsymbol{k}) + \sin\chi_{ev}(\boldsymbol{k})\cdot\mathscr{F}\{\varphi(\boldsymbol{r})\}(\boldsymbol{k}))$ [8,9,18], where $\chi_{ev}(\boldsymbol{k}) = (\chi(\boldsymbol{k}) + \chi(-\boldsymbol{k}))/2$ and $\chi_{odd}(\boldsymbol{k}) = (\chi(\boldsymbol{k}) - \chi(-\boldsymbol{k}))/2$ are even and odd parts of the aberration function $\chi(\boldsymbol{k})$, respectively. This pattern is limited by the lens aperture $A(\boldsymbol{k})$.

The full exit electron wave function $\psi^O(\boldsymbol{r}) = A_0(\boldsymbol{r})e^{i\varphi(\boldsymbol{r})}$, together with its *amplitude and phase*, can now be retrieved by using a SB aperture, *e.g.*, $A_{SB}(\boldsymbol{k}+\boldsymbol{q})$ centered at $\boldsymbol{k} = -\boldsymbol{q}$. The resulting expression takes the form

$$\mathscr{F}^{-1}\{I(\boldsymbol{r})\}(\boldsymbol{k})\cdot A_{SB}(\boldsymbol{k}+\boldsymbol{q}) = \mathscr{F}\left\{\psi^O(\boldsymbol{r})\right\}(\boldsymbol{k}+\boldsymbol{q})\cdot A_{SB}(\boldsymbol{k}+\boldsymbol{q})A(\boldsymbol{k}+\boldsymbol{q})e^{-i\chi(\boldsymbol{k}+\boldsymbol{q})}. \tag{10}$$

The remaining terms are no longer present because the SB aperture size is typically chosen such that there is no information from $\mathscr{F}\{I^{TEM}(\boldsymbol{r})\}(\boldsymbol{k})$ and $\mathscr{F}\{\overline{\psi^O(\boldsymbol{r})}\}(\boldsymbol{k}-\boldsymbol{q})$ within $A_{SB}(\boldsymbol{k}+\boldsymbol{q})$. If this criterion is not fulfilled, then there will be mixing of information between the central and SBs. The voltage applied to the biprism, which results in the tilt vector $\boldsymbol{q}$, plays a crucial role, together with the two apertures. By shifting the pattern in Eq. (9) by $\boldsymbol{q}$ back to the origin and applying another IFT, the final SB recovery formula is obtained as follows:

$$\begin{aligned}\psi_{SB}(\boldsymbol{r}) &= \mathscr{F}^{-1}\left\{\mathscr{F}^{-1}\{I(\boldsymbol{r})\}(\boldsymbol{k}-\boldsymbol{q})\cdot A_{SB}(\boldsymbol{k})\right\}(\boldsymbol{r}) \\ &= \mathscr{F}^{-1}\left\{\mathscr{F}\left\{\psi^{O}(\boldsymbol{r})\right\}(\boldsymbol{k})A_{SB}(\boldsymbol{k})A(\boldsymbol{k})e^{-i\chi(\boldsymbol{k})}\right\}(\boldsymbol{r}) = \left(\psi^{O}(\boldsymbol{r}')* \mathscr{F}^{-1}\left\{A_{SB}(\boldsymbol{k})A(\boldsymbol{k})e^{-i\chi(\boldsymbol{k})}\right\}(\boldsymbol{r}')\right)(\boldsymbol{r}) \\ &= \left(A_0(\boldsymbol{r}')e^{i\varphi(\boldsymbol{r}')}* \mathscr{F}^{-1}\left\{A_{SB}(\boldsymbol{k})A(\boldsymbol{k})e^{-i\chi(\boldsymbol{k})}\right\}(\boldsymbol{r}')\right)(\boldsymbol{r}),\end{aligned} \tag{11}$$

where the convolution theorem has been applied once more. The resulting complex wave function $\psi_{SB}(\boldsymbol{r})$, which has been obtained from the recorded hologram $I(\boldsymbol{r})$ with $\psi_{SB}(\boldsymbol{r}) = \mathscr{F}^{-1}\{\mathscr{F}^{-1}\{I(\boldsymbol{r})\}(\boldsymbol{k}-\boldsymbol{q})\cdot A_{SB}(\boldsymbol{k})\}(\boldsymbol{r})$, is directly interpretable *via* Eq. (11).

For an aberration-corrected microscope, $\chi(\boldsymbol{k}) \approx 0$ and the expression in Eq. (11) takes the form $\psi_{SB}(\boldsymbol{r}) = (A_0(\boldsymbol{r}')e^{i\varphi(\boldsymbol{r}')}* \mathscr{F}^{-1}\{A_{SB}(\boldsymbol{k})A(\boldsymbol{k})\}(\boldsymbol{r}'))(\boldsymbol{r})$, which is a low-pass-filtered version of the sample exit wave function $\psi^{O}(\boldsymbol{r}) = A_0(\boldsymbol{r})e^{i\varphi(\boldsymbol{r})}$, where the highest cut-off frequency is determined by the size of the smaller of the two apertures, *i.e.*, the SB aperture $A_{SB}(\boldsymbol{k})$ and the lens aperture $A(\boldsymbol{k})$. In an ideal case, if both apertures are of infinite size, reconstruction yields the exit electron wave function $\psi_{SB}(\boldsymbol{r}) = A_0(\boldsymbol{r})e^{i\varphi(\boldsymbol{r})}$ directly. If the aberrations are known, then it is straightforward to multiply $\mathscr{F}\{\psi_{SB}(\boldsymbol{r})\}(\boldsymbol{k})$ by $e^{i\chi(\boldsymbol{k})}$ to correct for them during post processing.

For a thin sample, the projected electrostatic potential $V_p(\boldsymbol{r})$ affects the phase of the passing electron wave [8,9,19] (a plane wave in TEM mode) *via* its transmission function $T(\boldsymbol{r}) = e^{i\varphi(\boldsymbol{r})}$ directly. For a non-magnetic sample $\varphi(\boldsymbol{r}) = \sigma V_p(\boldsymbol{r}) = \sigma\int_z V(\boldsymbol{r},\ z)dz$, where $\sigma = 2\pi me\lambda / h^2$ [19,25] and $e$, $m$ and $\lambda$ are the charge, relativistic mass, and relativistic wavelength of the electron, respectively. The question of when a sample can be considered thin is nontrivial [39]. At close-to-atomic spatial resolution or in the presence of strong diffraction contrast, only a few monolayers of a crystalline structure can be considered as thin, whereas for amorphous-like samples the thickness can be considerably larger. At medium spatial resolution, the approximation can often be extended to slowly-varying strong phase objects.

According to Gauss' law (one of Maxwell's equations), the projected electric field $\boldsymbol{E}_p(\boldsymbol{r}) = (E_x(\boldsymbol{r}), E_y(\boldsymbol{r}))$, which is a conservative vector field, is the negative of the gradient of the projected electrostatic potential $V_p(\boldsymbol{r})$, according to the expression

$$\boldsymbol{E}_p(\boldsymbol{r}) = -\nabla V_p(\boldsymbol{r}). \tag{12}$$

Therefore, after reconstruction of the phase using Eq. (10) or Eq. (11), the projected electric field vector can be obtained straightforwardly by applying the gradient operator $\nabla$.

### 3.2. 4D-STEM via DPC: theory of electrostatic potential and electric field measurement

For STEM, the imaging procedure involves 4D-STEM data acquisition and the determination of interpretable output *via* DPC mode. In this configuration (Figs. 2(c) and (d)), for a certain position of the probe $\boldsymbol{r}_p$ at the sample the electron wave function in the detector plane $\psi_D(\boldsymbol{k},\ \boldsymbol{r}_p)$ is a CBED pattern in the far field. The intensity of the electron wave function $I(\boldsymbol{k},\ \boldsymbol{r}_p) = |\psi_D(\boldsymbol{k},\ \boldsymbol{r}_p)|^2$, which takes the form of a two-dimensional CBED pattern, can be recorded either in full using a camera [31,32,34] or by using larger-segment-size detectors [25,33]. As the probe positions are specified in two-dimensional space, in total a 4D dataset is recorded: hence, the term 4D-STEM. Any type of STEM detector can be constructed virtually by post processing a dataset recorded using a camera.

As mentioned above, different techniques can be used to extract the projected electrostatic potential field of the sample from a 4D-STEM dataset. Here, we compute the COM of the CBED pattern to obtain a DPC-STEM vector image [25], according to the expressions

$$\boldsymbol{I}^{DPC}(\boldsymbol{r_p}) = \boldsymbol{I}^{COM}(\boldsymbol{r_p}) = \iint_{-\infty}^{\infty} \boldsymbol{k}\ I(\boldsymbol{k},\boldsymbol{r}_p)d^2\boldsymbol{k} \tag{13a}$$

$$\left(I^{COM_x}(\boldsymbol{r_p}),\ I^{COM_y}(\boldsymbol{r_p})\right) = \left(\iint_{-\infty}^{\infty} k_x\ I(\boldsymbol{k},\boldsymbol{r}_p)d^2\boldsymbol{k},\ \iint_{-\infty}^{\infty} k_y\ I(\boldsymbol{k},\boldsymbol{r}_p)d^2\boldsymbol{k}\right). \tag{13b}$$

In practice, the computation is performed over the camera pixels, $\boldsymbol{k}_p = (k_{px},\ k_{py})$ in discretized detector plane space $\boldsymbol{k} = (k_x, k_y)$ by using finite sums instead of integrals, for example in the form $I^{COM_x}(\boldsymbol{r_p}) = \sum_{k_y}\sum_{k_x} k_{px}\ I(\boldsymbol{k}_p,\boldsymbol{r}_p)$. This equation should include a normalization factor, such as $\iint_{-\infty}^{\infty} I(\boldsymbol{k},\boldsymbol{r}_p)\ d^2\boldsymbol{k}$ inEq. (13). In a theoretical expression, $\iint_{-\infty}^{\infty} I(\boldsymbol{k}\boldsymbol{r}_p)\ d^2\boldsymbol{k} = \iint_{-\infty}^{\infty} |\psi_D(\boldsymbol{k},\ \boldsymbol{r}_p)|^2 d^2\boldsymbol{k} = 1$, as the quantum mechanical electron wave function must be normalized. It should also be noted that, unlike in full 4D-STEM, only two values, $I^{COM_x}(\boldsymbol{r_p})$ and $I^{COM_y}(\boldsymbol{r_p})$, are obtained for each probe position to create two DPC-STEM component images.

For a thin sample [39], the projected electric field can be obtained directly without any further approximations. The DPC-STEM vector image described by Eq. (13) can be proven to reduce to the expression [24,25]

$$\boldsymbol{I}^{DPC}(\boldsymbol{r}_p) = \boldsymbol{I}^{COM}(\boldsymbol{r}_p) = \frac{1}{2\pi}\left(|\psi_{in}(\boldsymbol{r})|^2 \bigstar \nabla\varphi(\boldsymbol{r})\right)(\boldsymbol{r}_p), \tag{14}$$

where $\bigstar$ denotes cross correlation, $\psi_{in}(\boldsymbol{r})$ is the input convergent electron wave at the entrance of the sample, the focused probe can be placed anywhere in the sample plane $\boldsymbol{r_p}$ and $\varphi(\boldsymbol{r}) = \sigma V_p(\boldsymbol{r}) = \sigma\int_z V(\boldsymbol{r},\ z)dz$ is, as before, the phase of the transmission function of the sample $T(\boldsymbol{r}) = e^{i\varphi(\boldsymbol{r})}$. As each CBED pattern is measured in the far field, the forward relation between the input electron wave, the sample transmission function and the electron wave at the detector plane can be specified by using a FT [40] in the form

$$\psi_D(\boldsymbol{k},\ \boldsymbol{r}_p) = \mathscr{F}\{\psi_{in}(\boldsymbol{r})\ T(\boldsymbol{r}+\boldsymbol{r}_p)\}(\boldsymbol{k}) = \mathscr{F}\left\{\psi_{in}(\boldsymbol{r})\ e^{i\varphi(\boldsymbol{r}+\boldsymbol{r}_p)}\right\}(\boldsymbol{k}). \tag{15}$$

In combination with Eq. (13), this relation can be used to derive Eq. (14) [25].

The final COM image $\boldsymbol{I}^{COM}(\boldsymbol{r_p})$ is expressed as a cross correlation of the electron probe at the specimen and *the gradient, or differential, of the phase* of the transmission function of the specimen: hence, the name *differential phase contrast (DPC)* STEM - here $\boldsymbol{I}^{DPC}(\boldsymbol{r_p})$. For a non-magnetic sample, recalling Eq. (12), Eq. (14) can be written in the form

$$\boldsymbol{I}^{DPC}(\boldsymbol{r}_p) = \boldsymbol{I}^{COM}(\boldsymbol{r}_p) = \frac{\sigma}{2\pi}\left(|\psi_{in}(\boldsymbol{r})|^2 \bigstar (-\boldsymbol{E}_p(\boldsymbol{r}))\right)(\boldsymbol{r}_p), \tag{16}$$

showing that the COM signal is related linearly to the projected electric field $\boldsymbol{E}_p(\boldsymbol{r})$.

If the probe intensity $|\psi_{in}(\boldsymbol{r})|^2$ were to take the form of an ideal Dirac delta function, then the DPC-STEM image expression would reduce to $\boldsymbol{I}^{DPC}(\boldsymbol{r}_p) = \frac{-\sigma}{2\pi}\boldsymbol{E}_p(\boldsymbol{r}_p)$, becoming directly proportional to the projected electric field of the sample. For a well-tuned system, the probe wave function is given by the expression $\psi_{in}(\boldsymbol{r}) = \mathscr{F}\{A(\boldsymbol{k})e^{-i\chi(\boldsymbol{k})}\}(\boldsymbol{r})$, where $A(\boldsymbol{k})$ and $\chi(\boldsymbol{k})$ are the aperture function and aberration function of the condenser lens system, respectively [19,25]. If the microscope is probe corrected, such that $\chi(\boldsymbol{k}) \approx 0$, then the probe wave function becomes an Airy function, which is a good approximation to a Dirac delta function. If the aberrations of the probe are known, then they can be corrected by Fourier transforming Eq. (16) to yield

$$\mathscr{F}\{\boldsymbol{I}^{DPC}(\boldsymbol{r}_p)\}(\boldsymbol{k}_p) = -\frac{\sigma}{2\pi}\overline{\mathscr{F}\left\{|\psi_{in}(\boldsymbol{r})|^2\right\}}(\boldsymbol{k}_p)\cdot\mathscr{F}\{\boldsymbol{E}_p(\boldsymbol{r})\}(\boldsymbol{k}_p), \tag{17}$$

followed by division by the transfer function $CTF(\boldsymbol{k}) = \frac{-\sigma}{2\pi}\overline{\mathscr{F}\{|\psi_{in}(\boldsymbol{r})|^2\}}(\boldsymbol{k})$ [33]. This approach is possible as, for most well-behaved probes, $CTF(\boldsymbol{k})$ is positive definite up to the STEM cut-off frequency given by the CSA of the beam [18,25].

Eq. (16) can be related to the classical view of the DPC imaging process [25]. When no sample is present, the electron continues along its original path, whereas the projected in-plane electric field of a sample $\boldsymbol{E}_p(\boldsymbol{r})$ changes its trajectory due to an in-plane Lorentz force component $\boldsymbol{F}(\boldsymbol{r}) = -e\boldsymbol{E}_p(\boldsymbol{r}) = e\nabla V_p(\boldsymbol{r})$. The angle of deflection, or equivalently the shift of the electron on the detector, is a direct measurement of this force and hence of the projected in-plane electric field. Quantum mechanically, the situation can be described in terms of the average angle of the electron deflection (see Fig. 2(c)), or equivalently in terms of the average position of the electron on the detector, as described by the COM according to Eq. (13).

Unlike in OAEH, for which a direct measurement allows the projected electrostatic potential $V_p(\boldsymbol{r})$ to be measured and the electric field $\boldsymbol{E}_p(\boldsymbol{r})$ to be obtained *via* Eq. (12), the opposite situation applies in 4D-STEM *via* the DPC approach. The initial measurement provides the projected electric field first, according to Eq. (16). The projected electrostatic potential can then be obtained by inverting the gradient in Eq. (12). In practice, iDPC-STEM [24,25,33] uses Eq. (12) as guidance and applies the inverse gradient or direct integration to a measured DPC-STEM dataset to perform iDPC-STEM. The inverse gradient can be computed in the Fourier domain. Given that a vector DPC-STEM image $\boldsymbol{I}^{DPC}(\boldsymbol{r}_p)$ is the gradient of a scalar iDPC-STEM image $I^{iDPC}(\boldsymbol{r}_p)$, where $\boldsymbol{I}^{DPC}(\mathbf{r_p}) = \nabla I^{iDPC}(\mathbf{r_p})$, then by Fourier transforming

$$\mathscr{F}\{\boldsymbol{I}^{DPC}(\boldsymbol{r}_p)\}(\boldsymbol{k}_p) = \mathscr{F}\{\nabla I^{iDPC}(\boldsymbol{r}_p)\}(\boldsymbol{k}_p) = 2\pi i\boldsymbol{k}_p\cdot\mathscr{F}\{I^{iDPC}(\boldsymbol{r}_p)\}(\boldsymbol{k}_p), \tag{18}$$

where the property of the FT $\mathscr{F}\{\nabla f(\boldsymbol{r})\} = 2\pi i\boldsymbol{k}\cdot\mathscr{F}\{f(\boldsymbol{r})\}$ has been applied. For $\boldsymbol{k}_p \neq 0$

$$\begin{aligned}\mathscr{F}\{I^{iDPC}(\boldsymbol{r}_p)\}(\boldsymbol{k}_p) &= \frac{\boldsymbol{k}_p\cdot\mathscr{F}\{\boldsymbol{I}^{DPC}(\boldsymbol{r}_p)\}(\boldsymbol{k}_p)}{2\pi i|\boldsymbol{k}_p|^2}\\ &= \frac{\sigma}{2\pi}\overline{\mathscr{F}\left\{|\psi_{in}(\boldsymbol{r})|^2\right\}}(\boldsymbol{k}_p)\cdot\mathscr{F}\{V_p(\boldsymbol{r})\}(\boldsymbol{k}_p),\end{aligned} \tag{19}$$

where the right side has been obtained by inserting Eq. (14) in the form $\boldsymbol{I}^{DPC}(\boldsymbol{r}_p) = \frac{\sigma}{2\pi}(|\psi_{in}(\boldsymbol{r})|^2\star\nabla V_p(\boldsymbol{r}))(\boldsymbol{r}_p)$. An IFT results in the expression [24,25]

$$I^{iDPC}(\boldsymbol{r}_p) = \mathscr{F}^{-1}\left\{\frac{\boldsymbol{k}_p\cdot\mathscr{F}\{\boldsymbol{I}^{DPC}(\boldsymbol{r}_p)\}(\boldsymbol{k}_p)}{2\pi i|\boldsymbol{k}_p|^2}\right\}(\boldsymbol{r}_p) = \frac{\sigma}{2\pi}\left(|\psi_{in}(\boldsymbol{r})|^2\star V_p(\boldsymbol{r})\right)(\boldsymbol{r}_p), \tag{20}$$

which demonstrates a linear relationship between the iDPC-STEM image $I^{iDPC}(\boldsymbol{r}_p)$ (here obtained using integrated COM (iCOM), therefore also referred to as $I^{iCOM}(\boldsymbol{r}_p)$), and the projected electrostatic potential $V_p(\boldsymbol{r})$. In general, the left side of Eq. (20) can be applied to DPC-STEM images obtained using segmented detectors [24,25], yielding the same result for $V_p(\boldsymbol{r})$, albeit cross-correlated with a different point spread function instead of $|\psi_{in}(\boldsymbol{r})|^2$. For COM, if the probe were a Dirac delta function, the expression for the iDPC-STEM image would reduce to $I^{iDPC}(\boldsymbol{r}_p) = \frac{\sigma}{2\pi}V_p(\boldsymbol{r}_p)$, becoming directly proportional to the projected electrostatic potential of the sample. It should be noted that, as $I^{iDPC}(\boldsymbol{r}_p)$ represents the projected electrostatic potential, its value at $\boldsymbol{k}_p = 0$ can be chosen freely as it represents the reference point of the electrostatic potential field, which also can be chosen freely. If the aberrations of the probe are known then, just as for the electric field, they can be corrected by Fourier transforming Eq. (20) to give

$$\mathscr{F}\{I^{iDPC}(\boldsymbol{r}_p)\}(\boldsymbol{k}_p) = \frac{\sigma}{2\pi}\overline{\mathscr{F}\left\{|\psi_{in}(\boldsymbol{r})|^2\right\}}(\boldsymbol{k}_p)\cdot\mathscr{F}\{V_p(\boldsymbol{r})\}(\boldsymbol{k}_p), \tag{21}$$

followed by division by the contrast transfer function $CTF(\boldsymbol{k}) = \frac{\sigma}{2\pi}\overline{\mathscr{F}\{|\psi_{in}(\boldsymbol{r})|^2\}}(\boldsymbol{k})$, which is possible [33] because for most probes $\psi_{in}(\boldsymbol{r})$ the $CTF(\boldsymbol{k})$ is a well-behaved positive definite function.

### 3.3. Model for the projected electrostatic potential and electric field of a needle-shaped sample

The projected electrostatic potential $V_p(\boldsymbol{r})$ and electric field $\boldsymbol{E}_p(\boldsymbol{r})$ of an electrically-biased conducting needle-shaped sample can be approximated by a simple analytical model for a line charge distribution. Analytical expressions for (a) the electrostatic potential in the $z = 0$ plane and (b) the associated projected electrostatic potential $V_p(\boldsymbol{r}) = V_p(x,\ y)$ of a line of constant charge density in the perpendicular direction $z$ are given by the expressions

$$V(x,y,0) = \frac{K}{4\pi\epsilon_0}\left[ln\left(\frac{\sqrt{(a+y)^2+x^2}+a+y}{\sqrt{x^2+y^2}+y}\right) - \frac{a}{\sqrt{(x+x_D)^2+(y+y_D)^2}}\right] \tag{22a}$$

$$\begin{aligned}V_p(x,y) = \frac{K}{4\pi\epsilon_0}\Big[&-(a+y)\ln\left((a+y)^2+x^2\right)+y\ln\left(x^2+y^2\right)+2a\\ &+2x\tan^{-1}\left(\frac{y}{x}\right)-2x\tan^{-1}\left(\frac{a+y}{x}\right)+a\ln\left((x+x_D)^2+(y+y_D)^2\right)\Big],\end{aligned} \tag{22b}$$

where $K(y) = dQ/dy = const$ is the charge density of a segment of length $a$ lying between $(0, -a)$ and $(0,\ 0)$, with a compensating charge at an arbitrarily far position $(x_D, y_D)$ to ensure overall charge neutrality and the convergence of $V_p(\boldsymbol{r})$ [43,46,47]. Two conducting lines of constant charge density with opposite signs can be described by rotating and displacing the coordinate system shown in Eq. (22). The electric field can then be obtained as before by using Eq. (12).

### 3.4. Determination of the charge density of a needle-shaped sample from the projected electrostatic potential using model-based iterative reconstruction

In addition to the electrostatic potential $V(\boldsymbol{r})$ and electric field $\boldsymbol{E}(\boldsymbol{r})$ in three-dimensional space $\boldsymbol{r} = (x,\ y,\ z)$, the fundamental quantity that is required to produce the potential and field is the electric charge $Q$. When distributed in space, it is better represented by the charge density distribution $\rho(\boldsymbol{r})$, where $Q = \iiint_r \rho(\boldsymbol{r})d^3\boldsymbol{r}$. This description can include point charges represented by Dirac delta functions, *e.g.*, to describe the atomic core charge $\rho(\boldsymbol{r}) = Ze\delta(\boldsymbol{r})$ of each atom with atomic number $Z$, where the total charge $Q = \iint\int_{-\infty}^{\infty} Ze\delta(\boldsymbol{r})d^3\boldsymbol{r} = Ze$. In the model introduced in the previous section, a line charge density distribution

$K(y)$ with $Q = \int_{-a}^{0} K(y)dy$ is used as a simplified one-dimensional description. The corresponding electrostatic potential field in three-dimensional space is given *via* the Coulomb potential law, which can be expressed in terms of the charge density distribution in the form

$$V(\boldsymbol{r}) = \frac{1}{4\pi\epsilon_0} \iiint_{r'} \frac{\rho(\boldsymbol{r}')}{|\boldsymbol{r} - \boldsymbol{r}'|} d^3\boldsymbol{r}', \tag{23}$$

where $\boldsymbol{r}'$ runs over the charge-occupied volume and the reference point for the potential is chosen at infinity, such that $V(\boldsymbol{r}\rightarrow\infty) = 0$.

By using this relation, MBIR can be used to retrieve the charge density distribution of a needle-shaped sample from the corresponding electrostatic potential distribution. MBIR can be used to retrieve the distribution of either magnetic moments or charges in a specimen from an electron optical phase image [48,49]. Here, only the electrostatic contribution is considered. MBIR allows the charge density distribution $\rho(\boldsymbol{r})$ to be mapped *via* $V_p(x, y) = \int_{-\infty}^{\infty} V(\boldsymbol{r})dz$ onto a set of measured projected potentials by a function $\boldsymbol{F}$: $\mathbb{R}^n \mapsto \mathbb{R}^m$, which defines a forward model with $n = 3N_xN_yN_z$ retrieval targets and $m = N_bN_uN_v$ measurements, where $N_x$, $N_y$ and $N_z$ are the numbers of grid points along the $x$, $y$ and $z$ directions, $N_u$ and $N_v$ are the numbers of pixels of the measured projected potential with two-dimensional spatial coordinates $u$ and $v$, and $N_b$ is the number of measurements [43].

In terms of the forward model $\boldsymbol{F}()$, which includes the relationship between $\rho(\boldsymbol{r})$ and $V(\boldsymbol{r})$ given by Eq. (23) and the projection along the $z$ direction, $V_p(x, y) = \int_{-\infty}^{\infty} V(\boldsymbol{r})dz$ can be expressed by the vectorization

$$V_p(x, y) = \boldsymbol{F}(\rho(\boldsymbol{r})) \overset{\text{vectorization}}{\rightarrow} \boldsymbol{Y} = \boldsymbol{F}(\boldsymbol{X}), \tag{24}$$

where $\boldsymbol{X}$ and $\boldsymbol{Y}$ represent the vectorized form of $\rho(\boldsymbol{r})$ and the vectorized concatenation of all of the pixels in measured images of $V_p^M(x, y)$, respectively. The goal is to retrieve $\rho(\boldsymbol{r})$ from $V_p^M(x, y)$ by solving an inverse problem. However, this inverse problem is ill-posed and does not guarantee the existence of a unique solution, or even a single solution. The solution is typically approximated by solving the least squares minimization of a cost function of the form

$$C(\boldsymbol{X}) \equiv \| \boldsymbol{F}(\boldsymbol{X}) - \boldsymbol{Y} \|^2 + R_\lambda. \tag{25}$$

The cost function $C(\boldsymbol{X})$ can be minimized iteratively by mapping a solution $\rho(\boldsymbol{r})$ (or $\boldsymbol{X}$) onto a corresponding $V_p^M(x, y)$ (or $\boldsymbol{Y}$) using the forward model $\boldsymbol{F}(\boldsymbol{X})$ until a best fit for $\rho(\boldsymbol{r})$ is found, such that $V_p(x, y)$ is the closest possible approximation to $V_p^M(x, y)$. The *a priori* information that is specified about the sample and imaging conditions can include a known region where charges can exist and regions where an experimental phase image is trustworthy. A Tikhonov regularisator can be used to enforce physical or mathematical constraints [48,50]. Here, we use a 0th order Tikhonov regularisator, which takes the form of a simple Euclidean norm

$$R_\lambda = \lambda_c \| \boldsymbol{X} \|^2, \tag{26}$$

where the value of $\lambda_c$ is used to find a balance between compliance with the measurements (the first term in Eq. (25)) and adherence to the regularisation (the second term in Eq. (25)). The MBIR approach can also consider the influence of charges that lie outside the FOV by adding a fictitious charge density distribution in a region of buffer pixels around the border of each experimental image, in order to improve the reliability of the reconstruction of the charge density inside the FOV.

## 4. Experimental results

In this section, measurements of external electrostatic potentials and electric fields of electrically-biased conducting needles recorded using OAEH and 4D-STEM *via* DPC are presented. The results are compared between the two approaches (Section 4.1), as well as with a theoretical model of the fields (Sections 4.2 and 4.3) based on line charge segments. In addition, measurements of cumulative charge are presented (Section 4.4) and the effects of biprism voltage and orientation are discussed (Section 4.5).

### 4.1. Comparison of projected electrostatic potential and electric field measurements recorded using OAEH and 4D-STEM via DPC

Experimental measurements of the projected electrostatic potential $V_p(\boldsymbol{r})$ and electric field $\boldsymbol{E}_p(\boldsymbol{r})$ recorded from the electrically-biased Au needles using OAEH and 4D-STEM *via* DPC are compared with each other in Fig. 3. Physical quantities are obtained as explained in Section 3. For OAEH, the projected electrostatic potential $V_p(\boldsymbol{r}) = \varphi(\boldsymbol{r})/\sigma$ is first obtained from the reconstructed phase. The electric field is then computed from its gradient, according to Eq. (12) (Section 3.1). For 4D-STEM, by measuring the COM shifts of the CBED patterns using a camera, the projected electric field is first obtained directly *via* DPC-STEM according to Eq. (14). An inverted gradient operation (*i.e.*, vector field integration) is then used to obtain the electrostatic potential field *via* iDPC-STEM, according to Eq. (20) (Section 3.2).

The coordinate system in Figs. 3(a) and (b) is chosen such that the $E_y(\boldsymbol{r})$ component of the projected electric field $\boldsymbol{E}_p(\boldsymbol{r}) = (E_x(\boldsymbol{r}), E_y(\boldsymbol{r}))$ inferred from the electron holographic phase is aligned with the conductive needles (shown in grey), while the $E_x(\boldsymbol{r})$ component is perpendicular to the needles. Suprisingly, the measurements show that the magnitudes of $V_p(\boldsymbol{r})$ and $\boldsymbol{E}_p(\boldsymbol{r})$ are considerably smaller when measured using OAEH (Figs. 3(a) and (b)), when they are compared with 4D-STEM *via* DPC (Figs. 3(c) and (d)). Figs. 3(e) and (f) show line profiles plotted along the vertical (solid) and horizontal (dashed) directions. The line profiles were averaged over a width of 30 nm to increase the signal-to-noise ratio (SNR). They highlight significant discrepancies when $V_p(\boldsymbol{r})$ and $\boldsymbol{E}_p(\boldsymbol{r})$ are measured directly using the two techniques. Although the projected electrostatic potential increases linearly along the line between the needles for both OAEH and 4D-STEM, it increases more rapidly for 4D-STEM than for OAEH (Fig. 3(e)). In theory, the electrostatic potential should be constant half-way between the two needles. However, a deviation arises due to the slightly different shapes and sizes of the needles, their slight tilt with respect to the $y$ axis and their slight misalignment in the $x$ direction. Significantly, Fig. 3(f) shows that $\boldsymbol{E}_p(\boldsymbol{r})$ measured using 4D-STEM is larger by ~90 V when compared to that measured by OAEH in both directions. In order to better understand this discrepancy, we now present a comparison with the theoretical model of the electrostatic potential and electric field described in Section 3.3.

### 4.2. Comparison of measured projected electrostatic potential with the theoretical model

In this Section, the experimental measurements are compared with the projected electrostatic potential $V_p^{Th}(\boldsymbol{r})$ computed using a theoretical model based on line segments of constant charge density (see Section 3.3). Figs. 4(a) and (b) show the projected electrostatic potential $V_p(\boldsymbol{r})$ measured using both 4D-STEM *via* DPC and OAEH, as described in Section 4.1 and shown in Figs. 3(c) and (a), respectively. Fig. 4 shows equally-spaced contour lines, which are plotted over different intensity ranges. The large spacing of the contour lines in Fig. 4(b) indicates that $V_p^{OAEH}(\boldsymbol{r})$ measured using OAEH is smaller than $V_p^{DPC}(\boldsymbol{r})$ measured using

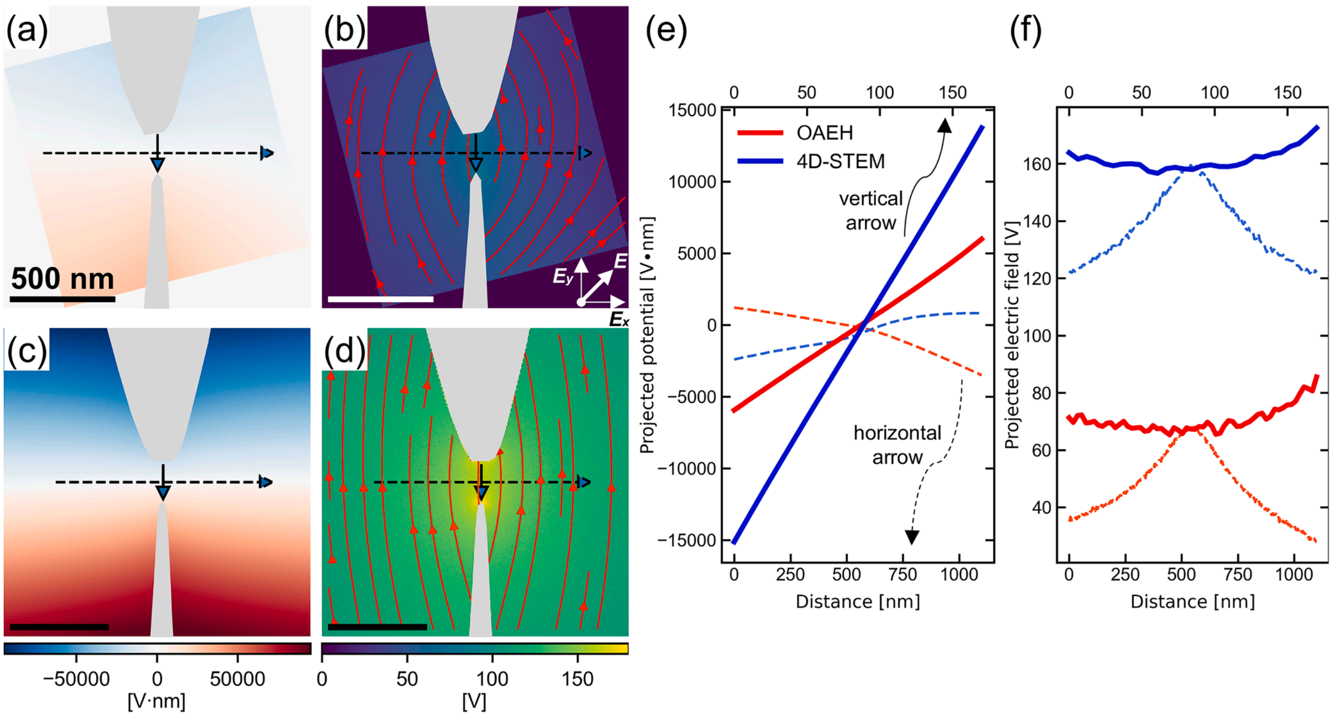

**Fig. 3.** Electrostatic potential and electric field measurements from two electrically-biased Au needles for (a, b) OAEH and (c, d) 4D-STEM *via* DPC. (a, c) Projected electrostatic potentials. (b, d) Projected electric fields, with projected electric field lines superimposed. The *xy* plane is perpendicular to the electron beam direction. The needles are marked in grey. (e, f) Line profiles of the projected electrostatic potential and electric field along the arrows marked in (a-d). OAEH is shown in red and 4D-STEM in blue. The solid and dashed line profiles are recorded along the solid and dashed arrows in the figures.

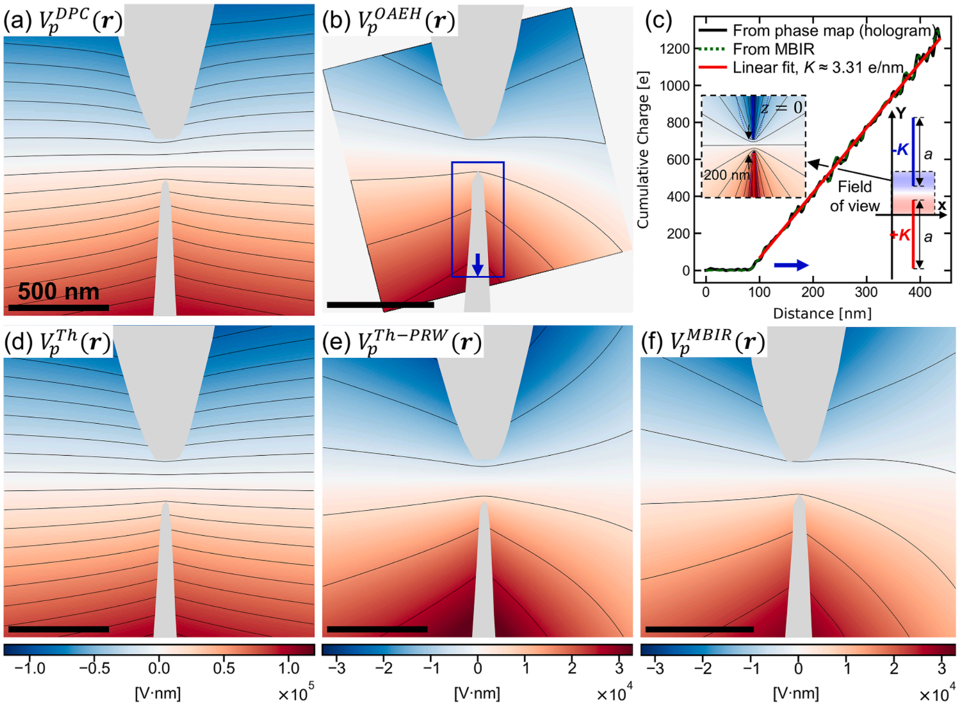

**Fig. 4.** Projected electrostatic potential around the biased needles (shaded in grey) recorded using (a) 4D-STEM *via* DPC and (b) OAEH. (c) Cumulative charge profile measured along the blue contour marked in (b) (black curve) and calculated from a charge density map obtained using MBIR (green-dashed curve). The blue arrow shows the direction in which the box increases. The red line is a linear fit to the cumulative charge profile. The inset on the right shows segments of line charge density $K$ and length $a$ used for calculating the projected electrostatic potential using a theoretical model. The inset on the left shows electrostatic equipotential lines computed around the line charges in the specimen plane ($z = 0$). The contours of the actual needles are indicated with blue dashed lines. (d, e) Projected electrostatic potential determined from the theoretical model (d) without and (e) with the inclusion of the PRW effect. (f) Projected electrostatic potential determined from the reconstructed projected charge density obtained using MBIR.

4D-STEM *via* DPC, which is shown in Fig. 4(a). It should be noted that the term $V_p(\boldsymbol{r})$ represents the projected electrostatic potential in general, while $V_p^{OAEH}(\boldsymbol{r})$ and $V_p^{DPC}(\boldsymbol{r})$ represent specifically the projected electrostatic potential measured experimentally using OAEH and 4D-STEM *via* DPC, respectively, while $V_p^{Th}(\boldsymbol{r})$ represents the projected electrostatic potential computed using a theoretical model according to Eq. (22b).

Interestingly, the difference between the OAEH and 4D-STEM measurements is not associated with an error in either approach. This point becomes evident when the results are compared to the theoretical model described in Section 3.3, which initially shows better agreement with the 4D-STEM *via* DPC than the OAEH measurements. In the theoretical calculation, the coordinates of the tips of the line segments are set to match the tips of the needles in the experimental images, as shown in Fig. 4(c). The inset to Fig. 4(c) shows a contour map of the electrostatic potential in the plane of the sample calculated from an analytical expression (Eq. (22a)) for two oppositely-charged lines, as shown schematically in Fig. 4(c). The fact that the equipotential surfaces around the line charges are nearly ellipsoids, which inherently resemble the shapes of the Au needles, confirms that the line segments generate a suitable solution for the electrostatic potential around the needles. A best-fitting theoretical model for $V_p^{DPC}(\boldsymbol{r})$ obtained from the 4D-STEM *via* DPC measurements was obtained based on Eq. (22b) by fitting the parameters $a$ and $K$ in the region outside the needles, resulting in values of 164 μm and 3.63 $e/nm$, respectively. Fig. 4(d) shows that the projected electrostatic potential $V_p^{Th}(\boldsymbol{r})$ calculated from the best-fitting theoretical model using Eq. (22b) closely matches $V_p^{DPC}(\boldsymbol{r})$ from the 4D-STEM measurements shown in Fig. 4(a).

In contrast, no amount of adjusting the model parameters $a$ and $K$ provided a good fit to the OAEH measurement shown in Fig. 4(b). Instead, the situation was resolved fully by subtracting a shifted image of the projected potential of the form $V_p^{Th}(\boldsymbol{r}+\boldsymbol{D})$, fitted to $V_p^{DPC}(\boldsymbol{r})$ as displayed in Fig. 4(d), in a direction perpendicular to the needle by a vector $\boldsymbol{D} = -D\boldsymbol{x}_o$, where $D > 0$ is an additional parameter representing the reference wave interference distance and

$$V_p^{Th-PRW}(\boldsymbol{r}) = V_p^{Th}(\boldsymbol{r}) \; - V_p^{Th}(\boldsymbol{r}+\boldsymbol{D}). \tag{27}$$

The new subtracted projected potential distribution $V_p^{Th-PRW}(\boldsymbol{r})$, which is shown in Fig. 4(e), agrees closely with the electrostatic potential $V_p^{OAEH}(\boldsymbol{r})$ measured using OAEH, which is shown in Fig. 4(b). This approach is required because of perturbation of the reference wave by the long-range electric field of the sample itself. Unlike for a neutral sample, the electrostatic potential field of the biased needle extends far into the vacuum, into the path of the reference wave (see the inset to Fig. 1(d) and Fig. 2(b)). The PRW then changes the phase recovered using OAEH [42–45].

At the position of the reference wave, the projected electrostatic potential is a shifted version of the projected electrostatic potential of the object $V_p(\boldsymbol{r}+\boldsymbol{D})$, centered at distance $D$ on the other side of the optical axis. Instead of being planar, the reference wave is a shifted version of the sample exit electron wave function $\psi^R(\boldsymbol{r}) = \psi^O(\mathbf{r}+\boldsymbol{D})$. The new reference wave at the detector plane (see Eq. (3b)) is

$$\begin{aligned}
\psi_D^R(\boldsymbol{r}) &= \mathscr{F}\left\{\mathscr{F}\left\{\psi^R(\boldsymbol{r})\right\}(\boldsymbol{k})\cdot A(\boldsymbol{k})e^{-i\chi(\boldsymbol{k})}\right\}(\boldsymbol{r})\\
&= \mathscr{F}\left\{\mathscr{F}\left\{\psi^0(\boldsymbol{r}+\boldsymbol{D})\right\}(\boldsymbol{k})\cdot A(\boldsymbol{k})e^{-i\chi(\boldsymbol{k})}\right\}(\boldsymbol{r})\\
&= \left(\psi^0(-\boldsymbol{r}'+\boldsymbol{D}) * \mathscr{F}\left\{A(\boldsymbol{k})e^{-i\chi(\boldsymbol{k})}\right\}(\boldsymbol{r}')\right)(\boldsymbol{r})'\\
&= \left(\left(A_0(-\boldsymbol{r}'+\boldsymbol{D})e^{i\varphi(-\boldsymbol{r}'+\boldsymbol{D})}\right) * \mathscr{F}\left\{A(\boldsymbol{k})e^{-i\chi(\boldsymbol{k})}\right\}(\boldsymbol{r}')\right)(\boldsymbol{r}).
\end{aligned} \tag{28}$$

The positions of the object and vacuum reference waves are shown in Fig. 5. The reference wave interference distance $D$ and the shadow width of the biprism $S$ were measured to be 2.8 μm and 0.16 μm, respectively, in our microscope setup at a biprism voltage of 140 V. The reference wave passes through vacuum on the left side of the needles, which results in a negative sign in the equation $\boldsymbol{D} = -D\boldsymbol{x}_o$.

The procedure described in Section 3.1 can be followed with the equations updated using Eq. (28). For an ideal lens, the hologram (see Eq. (6)) can be described by the expression

$$\begin{aligned}
I(\boldsymbol{r}) = {A_0}^2(-\boldsymbol{r}+D) + {A_0}^2(-\boldsymbol{r})\\
+2A_0(-\boldsymbol{r})A_0(-\boldsymbol{r}+\boldsymbol{D})\cos(2\pi\boldsymbol{q}\cdot\boldsymbol{r} + (\varphi(-\boldsymbol{r}) - \varphi(-\boldsymbol{r}+\boldsymbol{D}))),
\end{aligned} \tag{29}$$

in which both the amplitude and the phase are modified. Starting from Eq. (7) and applying a $\boldsymbol{q}$ shift and a SB aperture $A_{SB}(\boldsymbol{k})$, the reconstruction formula becomes

$$\begin{aligned}
\psi_{SB}(\boldsymbol{r}) &= \mathscr{F}^{-1}\left\{\mathscr{F}^{-1}\{I(\boldsymbol{r})\}(\boldsymbol{k}-\boldsymbol{q})\cdot A_{SB}(\boldsymbol{k})\right\}(\boldsymbol{r})\\
&= \left(\mathscr{F}^{-1}\left\{\mathscr{F}^{-1}\left\{\psi_D^O(\boldsymbol{r})\overline{\psi_D^R(\boldsymbol{r})}\right\}(\boldsymbol{k})\right\}(\boldsymbol{r}') * \mathscr{F}^{-1}\{A_{SB}(\boldsymbol{k})\}(\boldsymbol{r}')\right)(\boldsymbol{r})\\
&= \left(\psi_D^O(-\boldsymbol{r}')\overline{\psi_D^R(-\boldsymbol{r}')} * \mathscr{F}^{-1}\{A_{SB}(\boldsymbol{k})\}(\boldsymbol{r}')\right)(\boldsymbol{r})\\
&= \left(\left(\psi^0(\boldsymbol{r}) * \mathscr{F}^{-1}\left\{A(\boldsymbol{k})e^{-i\chi(\boldsymbol{k})}\right\}(\boldsymbol{r})\right)(\boldsymbol{r}')\cdot\overline{\left(\psi^0(\boldsymbol{r}+\boldsymbol{D}) * \mathscr{F}^{-1}\left\{A(\boldsymbol{k})e^{-i\chi(\boldsymbol{k})}\right\}(\boldsymbol{r})\right)}(\boldsymbol{r}') * \; \mathscr{F}^{-1}\{A_{SB}(\boldsymbol{k})\}(\boldsymbol{r}')\right)(\boldsymbol{r}),
\end{aligned} \tag{30}$$

where Eq. (1), Eq. (28) and the FT property $\mathscr{F}\{\mathscr{F}\{f(\boldsymbol{r})\}(\boldsymbol{k})\}(\boldsymbol{r}) = f(-\boldsymbol{r})$ have been used. If the reference wave $\psi^R(\boldsymbol{r})$ were $\psi^R(\boldsymbol{r}) = 1$ instead of $\psi^R(\boldsymbol{r}) = \psi^0(\boldsymbol{r}+\boldsymbol{D})$, then there would be no reference wave perturbation and Eq. (30) would reduce to Eq. (11).

In order to further interpret Eq. (30), it can be assumed that $A_{SB}(\boldsymbol{k})$ is smaller than $A(\boldsymbol{k})$ and the aberration function $\chi(\boldsymbol{k}) \approx 0$, such that $\mathscr{F}^{-1}\{A(\boldsymbol{k})e^{-i\chi(\boldsymbol{k})}\}(\boldsymbol{r}) \approx \delta(\boldsymbol{r})$ closely resembles a delta function. The simplified expression

$$\begin{aligned}
\psi_{SB}(\boldsymbol{r}) \approx \left(\psi^0(\boldsymbol{r}')\overline{\psi^0(\boldsymbol{r}'+\boldsymbol{D})} * \; \mathscr{F}^{-1}\{A_{SB}(\boldsymbol{k})\}(\boldsymbol{r}')\right)(\boldsymbol{r})\\
= \left(A_0(\boldsymbol{r}')A_0(\boldsymbol{r}'+\boldsymbol{D})e^{i(\varphi(\boldsymbol{r}')-\varphi(\boldsymbol{r}'+D))} * \; \mathscr{F}^{-1}\{A_{SB}(\boldsymbol{k})\}(\boldsymbol{r}')\right)(\boldsymbol{r})
\end{aligned} \tag{31}$$

then enables direct interpretation and the phase simply becomes

$$\varphi^{OAEH}(\boldsymbol{r}) = \varphi(\boldsymbol{r}) - \varphi(\boldsymbol{r}+\boldsymbol{D}), \tag{32}$$

where $\varphi^{OAEH}(\boldsymbol{r})$ is the phase of the sample exit wave function measured experimentally using OAEH. Eq. (27) can be then written in the more general form

$$V_p^{OAEH}(\boldsymbol{r}) = V_p(\boldsymbol{r}) \; - V_p(\boldsymbol{r}+\boldsymbol{D}). \tag{33}$$

It should be noted that, for a neutral sample in which the electrostatic potential and electric field are contained, when the distance $D$ is large enough $V_p(\boldsymbol{r}+\boldsymbol{D}) = 0$, $V_p^{OAEH}(\boldsymbol{r})$ reduces to $V_p(\boldsymbol{r})$ in Eq. (33) and OAEH yields the same result as 4D-STEM.

### *4.3. Comparison of measured projected electric field with the theoretical model*

The projected electric fields measured using the two experimental techniques were also compared with results obtained using the theoretical model. As the projected electrostatic potential and electric field

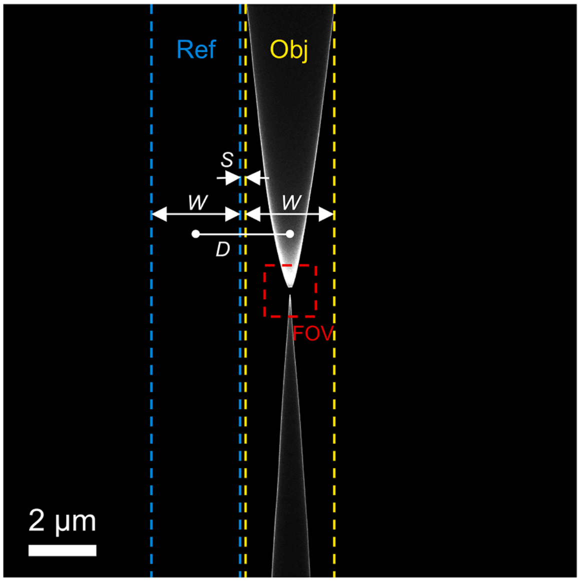

**Fig. 5.** ADF-STEM image of the Au needles showing the locations of the object and reference waves in OAEH. The object wave passes through the needles (the region between the yellow dashed lines), while the reference wave passes through vacuum (the region between the blue dashed lines). In the experiment, the FOV for OAEH and 4D-STEM *via* DPC is the region marked by a red dashed rectangle at the tips of the needles. The interference distance $D$ is proportional to the biprism voltage. The interference overlap width $W$ and the distance between the object and reference wave $S$ are indicated. The distance $S$ originates from the electron biprism shadow back-projected to the object plane.

are related by Eq. (12), for OAEH and the theoretical model the components of the projected electric field $\boldsymbol{E}_p(\boldsymbol{r})$ are obtained by calculating the gradients (derivatives) of the projected electrostatic potential. The application of a gradient operator to Eq. (33) results in the expression

$$\boldsymbol{E}_p^{OAEH}(\boldsymbol{r}) = \boldsymbol{E}_p(\boldsymbol{r}) - \boldsymbol{E}_p(\boldsymbol{r}+\boldsymbol{D}), \tag{34}$$

where $\boldsymbol{E}_p^{OAEH}(\boldsymbol{r})$ is the projected electric field measured using OAEH with the PRW included. For 4D-STEM *via* DPC, $\boldsymbol{E}_p^{DPC}(\boldsymbol{r})$ is measured directly, as explained in Section 3.2.

Fig. 6 shows the projected electric field $\boldsymbol{E}_p^{DPC}(\boldsymbol{r})$ measured using 4D-STEM *via* DPC, alongside $\boldsymbol{E}_p^{OAEH}(\boldsymbol{r})$ and $\boldsymbol{E}_p^{Th}(\boldsymbol{r})$ determined from OAEH and the theoretical model, respectively. All of the figures are displayed with the same intensity range to provide a direct comparison. The projected electric field computed from the theoretical model shown in Fig. 6(c) is in excellent agreement with that measured using 4D-STEM *via* DPC shown in Fig. 6(a). Consideration of the PRW effect in the theoretical model shown in Fig. 6(d) reproduces the projected electric field $\boldsymbol{E}_p^{OAEH}(\boldsymbol{r})$ measured using OAEH shown in Fig. 6(b). The projected electric field calculated from the charge density distribution in the needles determined using the MBIR approach, in which the PRW effect is already considered, is shown in Fig. 6(e).

In order to compare the projected electric field measured by the different methods in more detail, line profiles of $E_x(\boldsymbol{r})$ and $E_y(\boldsymbol{r})$ were generated along the vertical (solid) and horizontal (dashed) lines marked in Fig. 6. The values were averaged over a width of 30 nm along each line to improve the SNR. Figs. 7(a) and (c) show small differences in $E_x(\boldsymbol{r})$ measured using OAEH and 4D-STEM *via* DPC along the vertical and horizontal lines. Slight deviations from zero in $E_x(\boldsymbol{r})$, in particular for the experimental measurements, result from slight differences in the shapes and sizes of the needles, their slight tilt with respect to the $y$ axis and their slight misalignment in the $x$ direction.

In contrast, for $E_y(\boldsymbol{r})$ the 4D-STEM line profiles are larger by ~90 V than those from OAEH in both the vertical and the horizontal direction, similarly to the line profiles of $\boldsymbol{E}_p(\boldsymbol{r})$ shown in Fig. 3(f). The smaller magnitude of $\boldsymbol{E}_p^{OAEH}(\boldsymbol{r})$ originates primarily from the smaller $y$ component $E_y^{OAEH}(\boldsymbol{r})$ for OAEH. The theoretical model reproduces the components $E_x^{DPC}(\boldsymbol{r})$ and $E_y^{DPC}(\boldsymbol{r})$ from 4D-STEM closely for both the vertical and the horizontal lines. The theoretical model that includes the PRW effect also reproduces the $E_x^{OAEH}(\boldsymbol{r})$ and $E_y^{OAEH}(\boldsymbol{r})$ components from OAEH, confirming that the inclusion of the PRW in the theoretical model is able to account for the differences.

The large reduction in $E_y^{OAEH}(\boldsymbol{r})$ for OAEH, when compared to $E_y^{DPC}(\boldsymbol{r})$ measured using 4D-STEM, originates from the fact that the projected

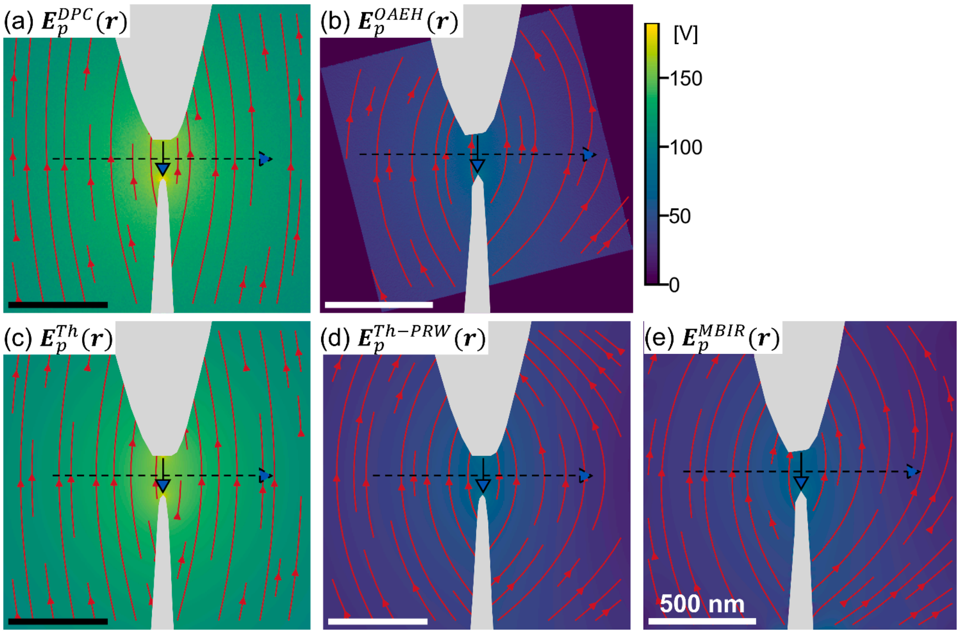

**Fig. 6.** (a, b) Projected electric field around the electrically-biased needles (marked in grey) recorded using (a) 4D-STEM *via* DPC and (b) OAEH. (c-e) Projected electric field calculated using the theoretical model (c) without and (d) with the PRW effect included and (e) using MBIR. These figures are derivatives of the projected electrostatic potentials shown in Figs. 4(d-f). The field contours are depicted by lines and arrows.

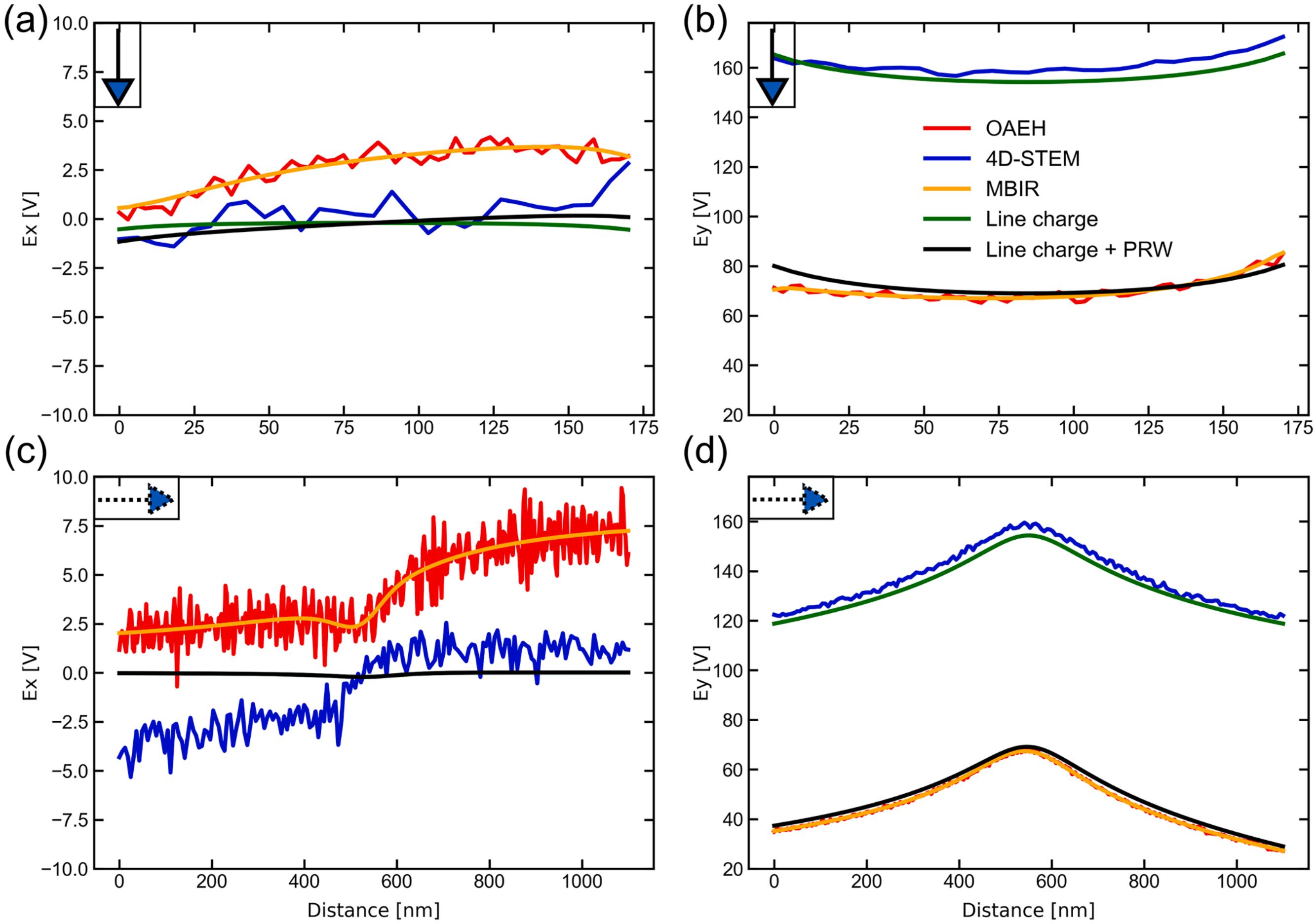

**Fig. 7.** Line profiles of (a, c) $E_x(\boldsymbol{r})$ and (b, d) $E_y(\boldsymbol{r})$ along the solid and dashed lines marked in Fig. 6 recorded using OAEH and 4D-STEM *via* DPC. Results obtained using MBIR and the theoretical line charge model are also included. The line profiles for 4D-STEM *via* DPC, OAEH, the line charge model, the line charge model including the PRW and MBIR are obtained from the lines marked in Figs. 6(a), (b), (c), (d) and (e), respectively.

electric field is oriented primarily parallel to the needles in the reference wave on both sides of the FOV (see Fig. 6(a)). Considering the slow decay of the projected electric field as a function of distance from the needle, the magnitude of $E_y(\boldsymbol{r})$ is significant even several μm from the needles, resulting in a decrease in $E_y^{OAEH}(\boldsymbol{r})$ according to Eq. (34). In contrast, the magnitude of $E_x(\boldsymbol{r})$ is small in the reference wave and $E_x^{OAEH}(\boldsymbol{r})$ is measured almost correctly. Subtraction of the slowly-decaying projected electric field in the reference wave from the symmetrical projected electric field in the object wave results in the slight asymmetry in the electric field observed in Fig. 6(b).

### 4.4. *Comparison between cumulative charge and line charge density measurements*

The cumulative charge along the Au needle was measured from the phase image recorded using OAEH, in order to calculate the line charge density and to compare it with the fitting parameter $K$ obtained from the theoretical model based on Section 3.3 and Eq. (33). The total charge $Q$ enclosed within an integration contour $C$ can be obtained by contour line integration of the gradient of the projected electrostatic potential according to the expression

$$Q = \epsilon_0 \oint_C \boldsymbol{E}_p(\boldsymbol{r}(s))\cdot\boldsymbol{n}(\boldsymbol{r}(s))ds = -\epsilon_0 \oint_C \nabla V_p(\boldsymbol{r}(s))\cdot\boldsymbol{n}(\boldsymbol{r}(s))ds, \qquad (35)$$

where $\epsilon_0$ is the permittivity of free space, $\nabla$ is a two-dimensional gradient operator, $\boldsymbol{r} = (x,y)$ is a two-dimensional vector in the specimen plane and $\boldsymbol{n}$ is an outward normal vector to a line parameter $s$ around the integration contour $C$ [51,52]. This approach was used to determine the cumulative charge profile along the lower needle by enlarging the size of the blue contour shown in Fig. 4(b) in the direction denoted by the arrow. The line charge density $K$ in the needle could then be calculated from the slope of the cumulative charge profile inside the needle, which was in turn determined from a best fitting line to the measured profile (Fig. 4(c)). The upper needle should ideally yield the same linear charge density, but with opposite sign. In practice, the linear charge densities in the upper and lower needles are slightly different due to their different shapes and sizes. The average of the line charge densities is $K = 3.31\ e/nm$, which is similar to the value of $K = 3.63\ e/nm$ obtained in Section 4.2.

The MBIR approach can also be used to determine the line charge density. The best-fitting solution for the projected charge density $\sigma_p^{MBIR}(x,\ y) = \int_{-\infty}^{\infty} \rho(x,y,z)dz$ (which should not be confused with the interaction constant, $\sigma = 2\pi me\lambda/h^2$ introduced in Section 3.1) was obtained by using the approach described in Section 3.4. The total charge $Q$ could be retrieved from a two-dimensional integral of the projected charge density $\sigma_p(x,\ y)$ over the region of interest, according to the expression [51,52]

$$Q = \int_{-\infty}^{\infty} dz \iint_C \rho(x,y,z)dxdy = \iint_C \sigma_p^{MBIR}(x,\ y)dxdy. \qquad (36)$$

The cumulative charge profile was then obtained from the projected charge density map along the lower needle in the region marked by a blue contour in Fig. 4(b). Fig. 4(c) shows that the cumulative charge profile calculated using the MBIR approach (green curve) exactly matches that calculated from the phase map using Eq. (35) (black curve), confirming that the line charge density $K$ obtained in Section 4.2 is reliable.

As mentioned above, the PRW effect was considered when estimating $V_p(\boldsymbol{r})$ using the theoretical model (Fig. 4(e)). In the MBIR approach, a fictitious charge density can be included in additional buffer pixels around the border of the FOV, as explained in Section 3.4. Fig. 4(f) shows $V_p^{MBIR}(\boldsymbol{r})$ calculated by using the forward model from the charge density, both from the needles inside the FOV and from the buffer region outside the FOV, which is almost the same as $V_p^{OAEH}(\boldsymbol{r})$ measured using OAEH in Fig. 4(b).

### 4.5. *Effect of biprism voltage and orientation*

In order to further explore the effect of the PRW on the OAEH measurements, the projected electrostatic potential $V_p^{OAEH}(\boldsymbol{r})$ and electric field $\boldsymbol{E}_p^{OAEH}(\boldsymbol{r})$ were measured around a single biased Au needle in the same manner as described above, but using different biprism voltages and orientations with respect to the needle. The biprism voltage was varied between 70 and 210 V in steps of 70 V for hologram acquisition. The interference distances $D$ were measured to be 1.4, 2.8 and 4.2 µm for biprism voltages of 70, 140 and 210 V, respectively. For this experiment, only the lower Au needle was biased at +50 V, while the upper needle was moved to the end of the holder. Two different orientations of the biprism with respect to the needle were chosen, with the biprism parallel (‖) and perpendicular (⊥) to the needle, resulting in the reference wave region being placed on the side of the needle (as shown in Fig. 5) or in front of the tip of the needle, respectively.

Figs. 8(a–c) show $\boldsymbol{E}_p^{DPC}(\boldsymbol{r})$ measured using 4D-STEM *via* DPC (Fig. 8(a)) and $\boldsymbol{E}_p^{OAEH}(\boldsymbol{r})$ measured using OAEH with a biprism voltage of 140 V and with the biprism oriented parallel (Fig. 8(b)) and perpendicular (Fig. 8(c)) to the needle. The magnitude of the projected electric field measured using OAEH in Figs. 8(b) and (c) is reduced by the PRW effect, when compared with the 4D-STEM measurement shown in Fig. 8(a). For the non-symmetrical situation, with the biprism placed alongside the needle, the projected electric field lines measured using OAEH in Fig. 8(b) are distributed asymmetrically around the needle due to the PRW effect. When the biprism is placed perpendicular to and in front of the needle, the situation is symmetrical and the field lines are distributed symmetrically in Fig. 8(c), just as in the 4D-STEM *via* DPC result shown in Fig. 8(a).

The projected electric fields measured using OAEH with different biprism voltages and orientations with respect to the needle are analysed in more detail in the form of line profiles of $E_x^{OAEH}(\boldsymbol{r})$ and $E_y^{OAEH}(\boldsymbol{r})$ in Figs. 8(d–g) along both the vertical (solid) and the horizontal (dashed) lines marked in Fig. 8(a). All of the line profiles were averaged over a width of 30 nm to improve the SNR. The solid line profiles correspond to OAEH measurements with the biprism parallel (‖) to the needle, while the dashed line profiles correspond to those with the biprism perpendicular (⊥) to the needle. Line profiles of $E_x^{DPC}(\boldsymbol{r})$ and $E_y^{DPC}(\boldsymbol{r})$ measured using 4D-STEM *via* DPC in Fig. 8(a) are also included for reference (black curves).

The line profiles shown in Fig. 8 exhibit similar trends to those shown in Fig. 7, in terms of asymmetry and reduction in $E_y^{OAEH}(\boldsymbol{r})$. However, for the single needle $E_x^{OAEH}(\boldsymbol{r})$ is not close to zero along the horizontal line for both biprism orientations in Fig. 8(e). This observation indicates that the $x$ component of $\boldsymbol{E}_p(\boldsymbol{r})$ is not negligible alongside the single needle, as shown in Fig. 8(a), in contrast to the two needles in Fig. 6. The presence of an $x$-component of $\boldsymbol{E}_p(\boldsymbol{r})$ next to the single needle in the reference wave also results in $E_x^{OAEH}(\boldsymbol{r})$ for the parallel biprism being ~10 V larger than $E_x(\boldsymbol{r})$ in Figs. 8(d) and (e). The magnitude of the $x$ component of $\boldsymbol{E}_p(\boldsymbol{r})$ in the reference wave for the parallel biprism orientation can be predicted from the line profile of the 4D-STEM measurement, which converges to 10 V on both sides of the needle in Fig. 8(e). In contrast, $E_x^{OAEH}(\boldsymbol{r})$ measured using OAEH with the perpendicular biprism

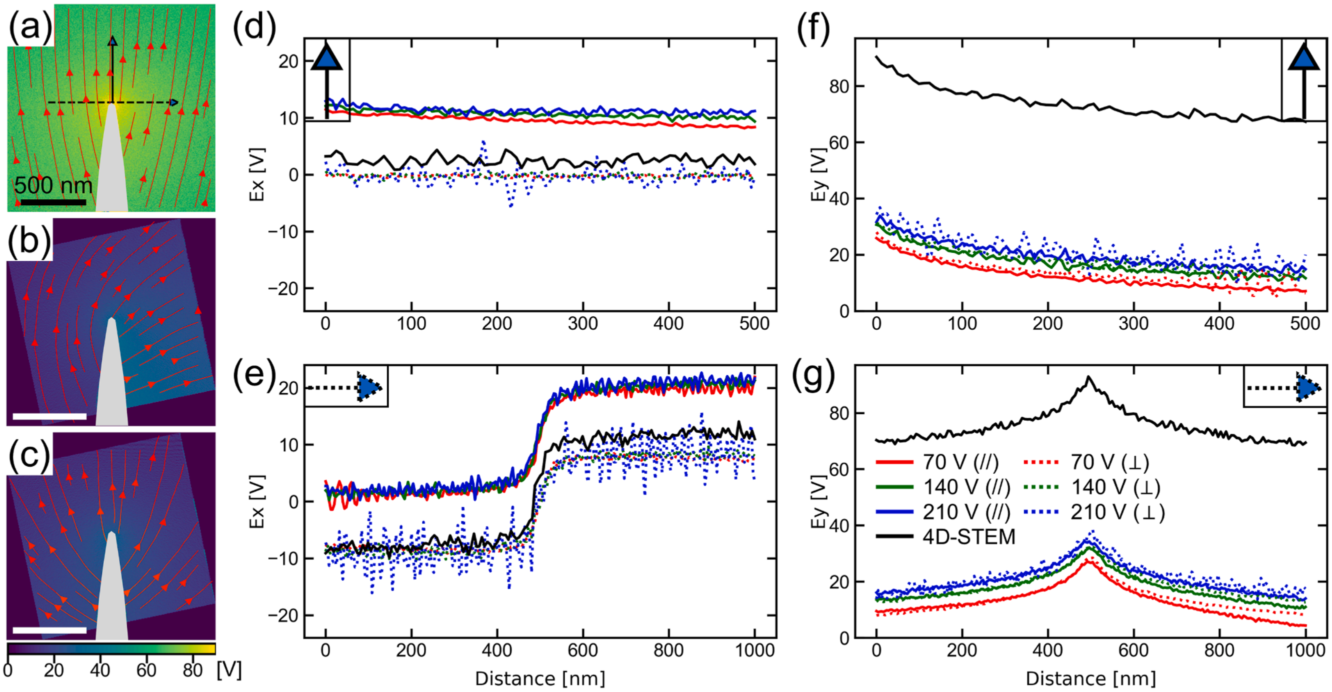

**Fig. 8.** Projected electric field measured using OAEH around a single electrically-biased Au needle (marked in grey) for two biprism orientations (parallel and perpendicular to the needle) and different biprism voltages. (a) Projected electric field measured using 4D-STEM *via* DPC as a reference. (b, c) Projected electric field measured using OAEH with the biprism (b) parallel (‖) and (c) perpendicular (⊥) to the needle. The biprism voltage is 140 V. The field is depicted using lines and arrows. (d, e) Line profiles of $E_x(\boldsymbol{r})$ and (f, g) line profiles of $E_y(\boldsymbol{r})$ obtained along the vertical solid and horizontal dashed arrows in (a–c), respectively, for two biprism orientations and biprism voltages of 70, 140 and 210 V.

orientation is close to $E_x^{DPC}(\boldsymbol{r})$ from 4D-STEM along the horizontal and vertical lines because the $x$ component of $\boldsymbol{E}_p(\boldsymbol{r})$ is almost zero a few μm from the needle in the direction parallel to the needle (see Fig. 8(a)).

In general, $E_y^{OAEH}(\boldsymbol{r})$ increases with biprism voltage. For a biprism voltage of 210 V, $E_y^{OAEH}(\boldsymbol{r})$ is ~10 V higher than for a biprism voltage of 70 V. As the interference distance $D$ increases with biprism voltage, the reference wave region moves away from the needle, thereby reducing the magnitude of the long-range electric field $\boldsymbol{E}_p(\boldsymbol{r}+\boldsymbol{D})$ and increasing $E_y^{OAEH}(\boldsymbol{r})$ according to Eq. (34). In contrast, $E_x^{OAEH}(\boldsymbol{r})$ does not change significantly, as the $x$ component of $\boldsymbol{E}_p(\boldsymbol{r})$ does not change significantly with distance from the needle for both biprism orientations in the present experimental setup. Further details about the acquisition of electron holograms using different biprism voltages are described in Appendix A.

$E_y^{OAEH}(\boldsymbol{r})$ measured using OAEH is approximately 50 V smaller for both biprism orientations than $E_y^{DPC}(\boldsymbol{r})$ measured using 4D-STEM. The reduction in $E_y^{OAEH}(\boldsymbol{r})$ is analogous to the difference between the measurements for the two biased needles in Figs. 7(b) and (d). The slight asymmetry in the solid lines in Fig. 8(g) is responsible for the asymmetry in the projected electric field lines in Fig. 8(b) due to the PRW effect.

## 5. Discussion

Measurement of the same physical entity using two different approaches increases confidence in the result and confirms the reliability of both techniques. The imaging of a neutral thin sample using electron holographic techniques and STEM, especially in DPC mode, yields reliable and closely matching results. This consistency is expected, as both techniques measure the phase of the transmission function of the sample. In the present work, the TEM mode of OAEH and 4D-STEM *via* DPC using the COM of CBED patterns have been used to measure the long-range electric fields of electrically-biased conducting needles. The measurements yield different results, which can be largely explained by perturbation of the reference wave in OAEH. This behaviour is explained using a theoretical treatment in Section 4.2. When the PRW is taken into account, the results match closely. In contrast to OAEH, 4D-STEM *via* DPC does not require the use of a reference wave to extract the electric field. Nevertheless, other important concerns remain. These concerns are discussed here for completeness and future reference.

The electric field of an electrically-biased conducting needle extends in-plane far enough to influence the reference electron wave in OAEH at a significant distance, suggesting that it also extends significantly in the direction of electron propagation. Consequently, treating the sample as thin becomes questionable for both OAEH and 4D-STEM *via* DPC. As OAEH is performed in conventional TEM mode using parallel illumination, the transmission function $T(\boldsymbol{r}) = e^{i\varphi(\boldsymbol{r})}$ of a thin sample cannot be applied to yield $\psi^O(\boldsymbol{r}) = 1\cdot e^{i\varphi(\boldsymbol{r})}$. Instead, the electron wave function can gain an amplitude modulation as well as a phase modulation. The relationship between the phase and the electrostatic potential $\varphi(\boldsymbol{r}) = \sigma\int_z V(\boldsymbol{r}, z)dz$ may also be affected [39]. Fortunately, the long-range electrostatic potential varies slowly outside the present samples and the projection approximation is still likely to hold [41].

The presence of an external electric field originating from a charge density distribution on the specimen holder and/ or the microscope column can also affect measurements of electric field. It is impossible to completely distinguish the electric field of the specimen from that originating from other objects in the microscope column. To a first approximation, OAEH is insensitive to external electric fields, since their contribution to the object wave is largely cancelled out by that in the reference wave, assuming that it is almost constant near the specimen. This point is explained further in Appendix C. In contrast, 4D-STEM *via* DPC is inherently sensitive to any external electric field present in the FOV. If the additional electric field is invariant over time and for different biasing setups in the vicinity of the FOV, then it can also be cancelled out by subtracting measurements recorded with 0 V applied to the needles from measurements recorded with a voltage applied to the needles for the case of 4D-STEM, as described in Section 2.

For 4D-STEM, care should be taken with electric field measurements due to drift of the transmitted disk over a long acquisition time, as well as when subtracting measurements recorded at different bias voltages at different times. Scan noise, dynamic specimen charging and specimen drift during the prolonged acquisition time are also inherent to STEM-based techniques. Furthermore, finite element and multislice simulations may be required for comparison with experimental results [53].

The PRW effect, which is the primary concern in the present paper, depends on the sample itself. An electrically-biased conducting sample produces a strong PRW effect, thereby causing a discrepancy in measurements recorded using OAEH. In contrast, for an electrically neutral sample that is not associated with an external electric field, measurements recorded using OAEH and 4D-STEM *via* DPC are likely to be almost identical, in the absence of artefacts such as those described in the previous paragraph or the influence of diffraction contrast in the sample. However, care is also required when examining dielectric (*i.e.*, insulating) samples, which can form electric fields outside them that can perturb the reference wave in OAEH as a result of electron-beam-induced specimen charging. Such electron-beam-induced charging effects can depend on the electrical properties of the material, the electron dose (rate) and the scan speed of the measurements.

## 6. Conclusions

Two different phase contrast techniques, OAEH and 4D-STEM *via* DPC, have been used to measure the projected electrostatic potential and electric field around electrically-biased conducting needles in the TEM. Results obtained using the two techniques were compared with each other and with a theoretical model based on line charges. Differences were observed in the magnitudes of the electric fields measured using OAEH and 4D-STEM *via* DPC. Comparisons with the theoretical model showed that 4D-STEM *via* DPC measurements provided more direct measurements of the electric field, whereas the OAEH results were affected by the long-range electric field outside the sample, which perturbs the vacuum reference wave and leads to an underestimation of the electrostatic potential and electric field. This effect was studied systematically for different biprism orientations and voltages. In contrast to regular electrically neutral (electric-field-space-confined) samples, the biased conducting needles exhibit extended electric fields, which reach the reference wave in OAEH. Inclusion of the electric field of the needle in a theoretical description of OAEH confirmed the observations. The charge density distributions in the needles were also determined from the measured projected potentials using MBIR and shown to match a simple theoretical model. In future studies, it may be possible to eliminate the PRW effect experimentally, for example by using a special electron optical setup [54–56]. However, in general, care should be taken when measuring long-range electric fields using a standard setup for OAEH. When considered in detail, both techniques provide results that are well understood and agree with each other. The present study highlights the benefit of comparing results obtained using complementary techniques, both with each other and with theoretical predictions.

## CRediT authorship contribution statement

**Janghyun Jo:** Writing – original draft, Visualization, Methodology, Investigation, Formal analysis, Data curation, Conceptualization. **Ivan Lazić:** Writing – review & editing, Validation, Supervision, Methodology, Investigation, Conceptualization. **Eric G.T. Bosch:** Writing – review & editing, Validation, Methodology, Investigation, Conceptualization. **Stefano Vespucci:** Writing – review & editing, Validation. **Giulio Pozzi:** Writing – review & editing, Validation. **Rafal E. Dunin-Borkowski:** Writing – review & editing, Validation, Supervision, Methodology, Investigation, Funding acquisition,

Conceptualization.

## Declaration of competing interest

The authors declare that they have no known competing financial interests or personal relationships that could have appeared to influence the work reported in this paper.

## Acknowledgement

This project has received funding from the European Union's Horizon Europe Research and Innovation Programme (Grant No. 101094299, project "IMPRESS").

## Appendix A

### *Perturbed reference wave effect on long-range electric field measurement in off-axis electron holography*

When measuring a long-range projected electrostatic potential or electric field using OAEH, the PRW effect can be reduced by using a higher biprism voltage, as shown in Fig. 8. However, this approach comes at the cost of decreasing the holographic fringe contrast and the SNR in the reconstructed phase. Fig. A.1 shows the SNR and root-mean-square (RMS) noise of $V_p(\boldsymbol{r})$ and $\boldsymbol{E}_p(\boldsymbol{r})$, respectively, measured using both 4D-STEM *via* DPC and OAEH for different biprism voltages and orientations. The SNR and RMS noise were measured in 150 nm × 150 nm areas of seven different regions around the single needle. The RMS noise was calculated after subtracting two-dimensional second-order polynomial fits from $V_p(\boldsymbol{r})$ and $\boldsymbol{E}_p(\boldsymbol{r})$ in each small region. Averaged values and standard deviations of the SNR and RMS noise are displayed in Fig. A.1. The SNR is always higher (and the RMS noise always lower) for the parallel than the perpendicular biprism orientation, since a parallel biprism corresponds to the most stable orientation in our microscope setup. The RMS noise increases (and the SNR decreases) with increasing biprism voltage because the holographic fringe contrast decreases due to the larger overlap width of the electron beam compared to its lateral coherence. The increase in RMS noise with increasing biprism voltage results in noise in the line profiles for a biprism voltage of 210 V in Fig. 8, illustrating the fact that a very high biprism voltage cannot be used to fully mitigate the PRW effect. Conversely, at a biprism voltage of 70 V Fresnel fringes originating from the edges of the biprism are present in the FOV and increase the RMS noise for both biprism orientations. The RMS noise in the 4D-STEM measurements is close to that measured for OAEH with a parallel biprism and biprism voltages of 140 and 210 V. Although the SNR of the 4D-STEM measurements appears to be higher than for OAEH, this difference results primarily from the lower magnitudes of $V_p^{OAEH}(\boldsymbol{r})$ and $\boldsymbol{E}_p^{OAEH}(\boldsymbol{r})$ originating from the PRW effect in OAEH.

## Appendix B

### *Electrostatic potential and electric field of a needle-shaped sample based on a line charge model*

A theoretical model based on line charges was used extensively in the present work to quantitatively evaluate the OAEH and 4D-STEM measurements, since it provides suitable solutions for conducting needle-shaped specimens that have ellipsoidal surfaces. In practice, the outer surfaces of the upper and lower needles shown in the inset to Fig. 4(c) do not have exactly ellipsoidal equipotential surfaces after electrochemical etching. In order to approximate $V_p(\boldsymbol{r})$ and $\boldsymbol{E}_p(\boldsymbol{r})$ for a needle that does not have an exactly ellipsoidal surface, an *effective* length and line charge density of the line segments should be introduced into the theoretical model. Figs. B.1 and B.2 show line profiles of $\boldsymbol{E}_p^{Th}(\boldsymbol{r})$ simulated using a theoretical model that comprises two charged line segments of different length $a$ and line charge density $K$. The solid and dashed line profiles represent the distribution of electric field around the needles without and with the PRW effect, respectively. By extending $a$ outwards from the FOV and varying $K$, the magnitude and local distribution of $\boldsymbol{E}_p^{Th}(\boldsymbol{r})$ (solid line) are changed around the tips of the line segments. The parameters $a$ and $K$ can be adjusted to achieve best fits of Eq. (22b) to measurements of $V_p(\boldsymbol{r})$. The fitting parameters $a$ and $K$ obtained from the best-fitting model in Fig. 4 can be regarded as *effective* values of $a$ and $K$. The *effective* values of $K$ and in particular $a$ do not have to be identical to the actual length and line charge density of the needle. Fig. B.3(a) shows $V(x, y, 0)$ obtained from Eq. (22a) for input parameters of $a = 1$ mm and $K = 3.31\ e/nm$, which are the actual length and line charge density of the needle, respectively. Figs. B.3(b) and (c) show line profiles of $E_y(\boldsymbol{r})$, the $y$-component of $\boldsymbol{E}_p(\boldsymbol{r})$, along the horizontal and vertical arrows in the middle of the needles, in the same manner as in Figs. 6 and 7. The use of the actual values of $a$ and $K$ (green curve) overestimates $\boldsymbol{E}_p(\boldsymbol{r})$ around the needles, when compared with $\boldsymbol{E}_p^{DPC}(\boldsymbol{r})$ measured experimentally using 4D-STEM (blue curve). A better fit can be obtained by decreasing $a$ to an *effective* value of $a$, which allows for considering the smaller magnitude of the electric field created by the true needle shape far from the FOV. However, the use of too many effective parameters in the theoretical model does not always provide better results. Figs. B.3(d–f) show $V(x, y, 0)$ simulated using the theoretical model and corresponding line plots of $E_y(\boldsymbol{r})$, the $y$-component of $\boldsymbol{E}_p(\boldsymbol{r})$, along the horizontal and vertical arrows in the middle of the needles, respectively. The $x$ and $y$ coordinates of both line segments and the values of $a$ and $K$ were used as fitting parameters to take into account the horizontal misalignment and non-ideal ellipsoidal shape of the needles. Fits over the whole area outside the needles using these four parameters result in a slightly better fit than that with only two parameters $a$ and $K$ in Fig. 4. However, the local distribution of $\boldsymbol{E}_p^{Th}(\boldsymbol{r})$ close to the tips of the needles is significantly different from the measurements obtained using 4D-STEM and OAEH, as shown in Figs. B.3(e) and (f). In this case, the large displacement of the line segments in the $x$ and $y$ directions does not physically make sense.

Although the present theoretical model is mathematically elegant, it may be too simple to represent all of the details in real experiments, such as a non-ellipsoidal needle surface. The model can be improved by introducing multiple line charges to model an arbitrary needle shape [57]. A variable line charge density along the needle may also be required [58]. In addition, care may be needed to select appropriate free parameters and corresponding fitting values. Nevertheless, it is still valuable to use such a simple model to predict $V_p(\boldsymbol{r})$ and $\boldsymbol{E}_p(\boldsymbol{r})$ around symmetrical well-aligned needle-shaped specimens, when compared to running time-consuming numerical simulations. Furthermore, the inclusion of the PRW effect into the simulated potential reproduces the reduced magnitude of the projected potential measured using OAEH.

## Appendix C

### *Long-range electrostatic potential and field measurement using OAEH and 4D-STEM*

Another aspect of the difference between OAEH and 4D-STEM can be seen in Fig. B.1. After including the PRW effect (dashed curve), $E_y^{Th}(\boldsymbol{r})$ is insensitive to $a$ except when $a$ is small (comparable to the size of the FOV), whereas without including the PRW effect (solid curve) $E_y^{Th}(\boldsymbol{r})$ increases logarithmically with $a$ around the charged line segments. This behaviour highlights the fact that OAEH is sensitive primarily to the local electric field near the FOV when including the PRW effect, whereas 4D-STEM is sensitive to the entire electric field resulting from charges far from the FOV, *e.g.,* on the specimen holder and microscope column, as well as to long-range magnetic fields in the microscope. Charge distributions far from the FOV contribute to an almost linear $V_p(\boldsymbol{r})$ and almost constant $E_y(\boldsymbol{r})$ in the vicinity of the FOV [57], which are almost removed by the reference wave in OAEH. In contrast, variations in electric field close to the needle tip are different in the object and reference waves and are not cancelled out readily in the same way, allowing OAEH to detect local information in the vicinity of the FOV. Electrostatic equipotential lines around the tips of the needles are similar to the inset to Fig. 4(c), with $a$ ranging from $10^{-5}$ to $10^{-2}$ m, resulting in invariance of the OAEH measurements in Fig. B.1. In contrast, the inset to Fig. B.1(c) shows that the smallest value of $a$, $10^{-6}$ m, changes the distribution and magnitude of the local electric field in the FOV due to the small size of $a$ when compared to the FOV, resulting in the discrepancy in the line profiles (dashed red curves) in Figs. B.1(b) and (d).

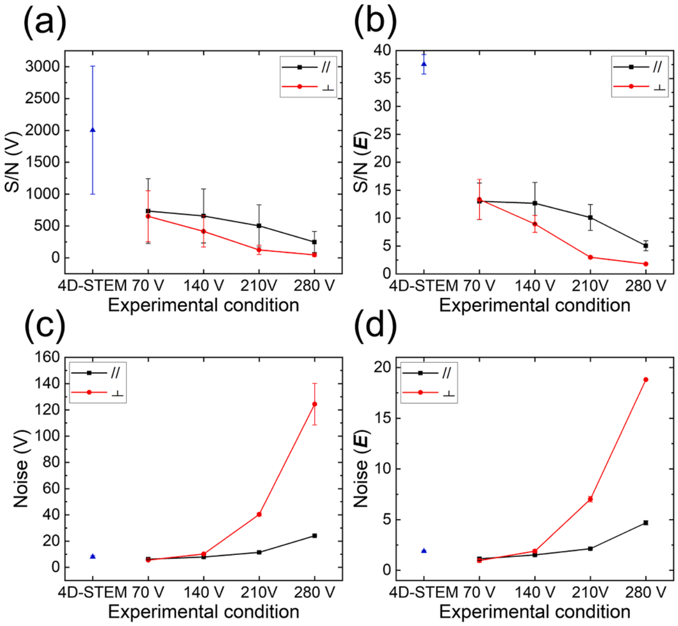

**Fig. A.1.** SNR and RMS noise of the projected electrostatic potential and electric field measured using 4D-STEM *via* DPC and OAEH for different biprism voltages and orientations. (a) SNR of the projected electrostatic potential. (b) SNR of the projected electric field. (c) RMS noise of the projected electrostatic potential. (d) RMS noise of the projected electric field. The error bars indicate the standard deviations of the measurements.

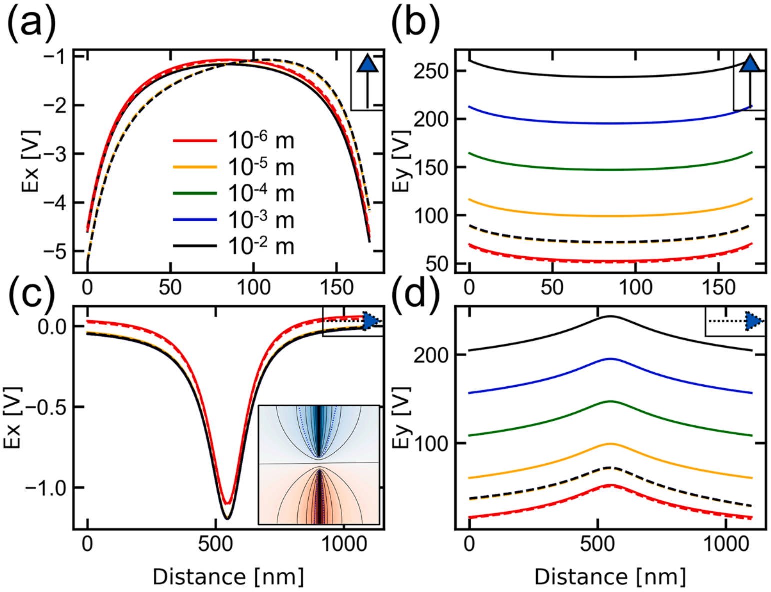

**Fig. B.1.** Line profiles of $E_x^{Th}(\boldsymbol{r})$ and $E_y^{Th}(\boldsymbol{r})$ computed using the theoretical model for different lengths of the line charges $a$. Line profiles of (a, c) $E_x^{Th}(\boldsymbol{r})$ and (b, d) $E_y^{Th}(\boldsymbol{r})$ are shown along the vertical and horizontal lines marked in Fig. 6, respectively. The solid and dashed line profiles correspond to the projected electric field calculated using Eq. (22b) and Eq. (12) without and with including the PRW effect, respectively. The inset in (c) shows electrostatic equipotential lines around the line charges in the specimen plane ($z = 0$) for $a = 1$ $\mu m$. The line charge density $K$ is fixed to 3.31 $e/nm$.

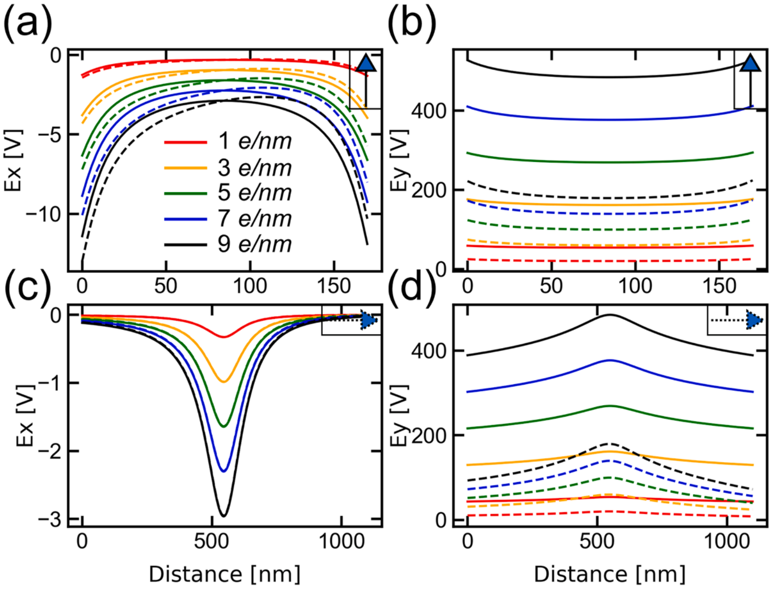

**Fig. B.2.** Line profiles of $E_x^{Th}(\boldsymbol{r})$ and $E_y^{Th}(\boldsymbol{r})$ computed using the theoretical model for different line charge densities $K$. Line profiles of (a, c) $E_x^{Th}(\boldsymbol{r})$ and (b, d) $E_y^{Th}(\boldsymbol{r})$ are shown along the vertical and horizontal lines marked in Fig. 6, respectively. The solid and dashed line profiles correspond to the projected electric field calculated using Eq. (22b) and Eq. (12) without and with including the PRW effect, respectively. The length of the line charge $a$ is fixed to 1 mm.

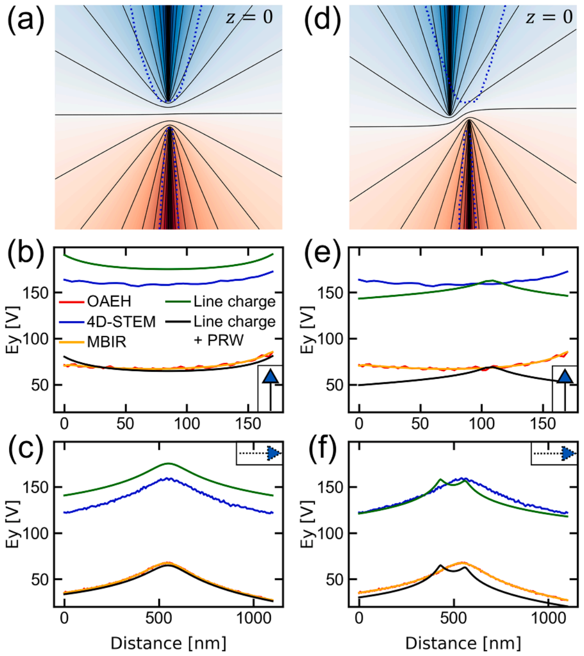

**Fig. B.3.** Line profiles of $E_y^{Th}(\boldsymbol{r})$ for different parameters of the theoretical model. (a) Electrostatic equipotential lines around the charged line segments in the specimen plane ($z = 0$) for $a = 1$ mm and $K = 3.31\ e/nm$. (b, c) $E_y(\boldsymbol{r})$ recorded along (b) the vertical and (c) the horizontal lines marked in Fig. 6, respectively. (d–f) The same datasets with the positions of the needles included as additional parameters for fitting of the theoretical model to the experimental data. The fitting parameters are $a = 998$ μm and $K = 2.76\ e/nm$. The blue-dashed lines in (a) and (d) mark the outer surfaces of the needles. The line profiles for OAEH, 4D-STEM *via* DPC, and MBIR are the same as those in Figs. 6 and 7.

## Data availability

Data will be made available on request.

## References

[1] H. Schmid, H.W. Fink, Carbon nanotubes are coherent electron sources, Appl. Phys. Lett. 70 (1997) 2679–2680, https://doi.org/10.1063/1.118978.

[2] R.B. Sharma, V.N. Tondare, D.S. Joag, A. Govindaraj, C.N.R. Rao, Field emission from carbon nanotubes grown on a tungsten tip, Chem. Phys. Lett. 344 (2001) 283–286, https://doi.org/10.1016/S0009-2614(01)00822-3.

[3] C.B. Carter, D.B. Williams, Transmission Electron Microscopy A Textbook For Materials Science, Springer, 2009.

[4] T.F. Kelly, D.J. Larson, Atom Probe Tomography 2012, Annu. Rev. Mater. Res. 42 (2012) 1–31, https://doi.org/10.1146/annurev-matsci-070511-155007.

[5] R.E. Dunin-Borkowski, M.R. McCartney, B. Kardynal, S.S.P. Parkin, M. R. Scheinfein, D.J. Smith, Off-axis electron holography of patterned magnetic nanostructures, J. Microsc. 200 (2000) 187–205, https://doi.org/10.1046/j.1365-2818.2000.00753.x.

[6] A.C. Twitchett, R.E. Dunin-Borkowski, P.A. Midgley, Quantitative electron holography of biased semiconductor devices, Phys. Rev. Lett. 88 (2002) 238302, https://doi.org/10.1103/PhysRevLett.88.238302.

[7] A.C. Twitchett, R.E. Dunin-Borkowski, R.F. Broom, P.A. Midgley, Quantitative electron holography of biased semiconductor devices, J. Phys.-Condens. Mat. 16 (2004) S181–S192, https://doi.org/10.1088/0953-8984/16/2/021.

[8] P.W. Hawkes, E. Kasper, Principles of Electron optics: Wave Optics, Academic press, 1996.

[9] H. Kohl, L. Reimer, Transmission Electron Microscopy, Springer, 2008.

[10] M.R. McCartney, D.J. Smith, Electron holography: phase imaging with nanometer resolution, Annu. Rev. Mater. Res. 37 (2007) 729–767, https://doi.org/10.1146/annurev.matsci.37.052506.084219.

[11] H. Lichte, M. Lehmann, Electron holography - basics and applications, Rep. Prog. Phys. 71 (2008) 016102, https://doi.org/10.1088/0034-4885/71/1/016102.

[12] C.T. Koch, A. Lubk, Off-axis and inline electron holography: a quantitative comparison, Ultramicroscopy 110 (2010) 460–471, https://doi.org/10.1016/j.ultramic.2009.11.022.

[13] T. Latychevskaia, P. Formanek, C.T. Koch, A. Lubk, Off-axis and inline electron holography: experimental comparison, Ultramicroscopy 110 (2010) 472–482, https://doi.org/10.1016/j.ultramic.2009.12.007.

[14] A. Lubk, F. Röder, Phase-space foundations of electron holography, Phys. Rev. A 92 (2015) 033844, https://doi.org/10.1103/PhysRevA.92.033844.

[15] T. Niermann, M. Lehmann, Holographic focal series: differences between inline and off-axis electron holography at atomic resolution, J. Phys. D Appl. Phys. 49 (2016) 194002, https://doi.org/10.1088/0022-3727/49/19/194002.

[16] C. Ozsoy-Keskinbora, C.B. Boothroyd, R.E. Dunin-Borkowski, P.A. van Aken, C. T. Koch, Mapping the electrostatic potential of Au nanoparticles using hybrid electron holography, Ultramicroscopy 165 (2016) 8–14, https://doi.org/10.1016/j.ultramic.2016.03.007.

[17] E. Karim, B. Park, C. Marcelot, V. Soldan, S. Balor, S. Bals, A. Le Forestier, C. Plisson-Chastang, C. Gatel, P.E. Gleizes, E. Snoeck, In-line and off-axis electron holography for the study of biological specimens, Microsc. Microanal. (2023) 1015–1016, https://doi.org/10.1093/micmic/ozad104.

[18] E.G.T. Bosch, I. Lazić, Analysis of HR-STEM theory for thin specimen, Ultramicroscopy 156 (2015) 59–72, https://doi.org/10.1016/j.ultramic.2015.02.004.

[19] E.J. Kirkland, Advanced Computing in Electron Microscopy, Springer, Cham, 2020.

[20] H. Rose, Nonstandard imaging methods in electron-microscopy, Ultramicroscopy 2 (1977) 251–267, https://doi.org/10.1016/S0304-3991(76)91538-2.

[21] E.M. Waddell, J.N. Chapman, Linear imaging of strong phase objects using asymmetrical detectors in stem, Optik 54 (1979) 83–96.

[22] N. Shibata, S.D. Findlay, Y. Kohno, H. Sawada, Y. Kondo, Y. Ikuhara, Differential phase-contrast microscopy at atomic resolution, Nat. Phys. 8 (2012) 611–615, https://doi.org/10.1038/NPHYS2337.

[23] K. Muller, F.F. Krause, A. Beche, M. Schowalter, V. Galioit, S. Loffler, J. Verbeeck, J. Zweck, P. Schattschneider, A. Rosenauer, Atomic electric fields revealed by a quantum mechanical approach to electron picodiffraction, Nat. Commun. 5 (2014) 5653, https://doi.org/10.1038/ncomms6653.

[24] I. Lazić, E.G.T. Bosch, S. Lazar, Phase contrast STEM for thin samples: integrated differential phase contrast, Ultramicroscopy 160 (2016) 265–280, https://doi.org/10.1016/j.ultramic.2015.10.011.

[25] I. Lazić, E.G.T. Bosch, Analytical review of direct stem imaging techniques for thin samples, Adv. Imag. Elect. Phys. 199 (2017) 75–184, https://doi.org/10.1016/bs.aiep.2017.01.006.

[26] P.W. Hawkes, J.C. Spence, Springer Handbook of Microscopy, Springer, Cham, 2019.

[27] P.D. Nellist, B.C. McCallum, J.M. Rodenburg, Resolution beyond the information limit in transmission electron-microscopy, Nature 374 (1995) 630–632, https://doi.org/10.1038/374630a0.

[28] A.M. Maiden, J.M. Rodenburg, An improved ptychographical phase retrieval algorithm for diffractive imaging, Ultramicroscopy 109 (2009) 1256–1262, https://doi.org/10.1016/j.ultramic.2009.05.012.

[29] M.J. Humphry, B. Kraus, A.C. Hurst, A.M. Maiden, J.M. Rodenburg, Ptychographic electron microscopy using high-angle dark-field scattering for sub-nanometre resolution imaging, Nat. Commun. 3 (2012) 730, https://doi.org/10.1038/ncomms1733.

[30] Y. Jiang, Z. Chen, Y.M. Hang, P. Deb, H. Gao, S.E. Xie, P. Purohit, M.W. Tate, J. Park, S.M. Gruner, V. Elser, D.A. Muller, Electron ptychography of 2D materials to deep sub-angstrom resolution, Nature 559 (2018) 343–349, https://doi.org/10.1038/s41586-018-0298-5.

[31] H. Ryll, M. Simson, R. Hartmann, P. Holl, M. Huth, S. Ihle, Y. Kondo, P. Kotula, A. Liebel, K. Muller-Caspary, A. Rosenauer, R. Sagawa, J. Schmidt, H. Soltau, L. Struder, A pnCCD-based, fast direct single electron imaging camera for TEM and STEM, J. Instrum. 11 (2016) P04006, https://doi.org/10.1088/1748-0221/11/04/P04006.

[32] M.W. Tate, P. Purohit, D. Chamberlain, K.X. Nguyen, R. Hovden, C.S. Chang, P. Deb, E. Turgut, J.T. Heron, D.G. Schlom, D.C. Ralph, G.D. Fuchs, K.S. Shanks, H. T. Philipp, D.A. Muller, S.M. Gruner, High dynamic range pixel array detector for scanning transmission electron microscopy, Microsc. Microanal. 22 (2016) 237–249, https://doi.org/10.1017/S1431927615015664.

[33] E. Yücelen, I. Lazić, E.G.T. Bosch, Phase contrast scanning transmission electron microscopy imaging of light and heavy atoms at the limit of contrast and resolution, Sci. Rep. 8 (2018) 2676, https://doi.org/10.1038/s41598-018-20377-2.

[34] T.J. Pennycook, A.R. Lupini, H. Yang, M.F. Murfitt, L. Jones, P.D. Nellist, Efficient phase contrast imaging in STEM using a pixelated detector. Part 1: experimental demonstration at atomic resolution, Ultramicroscopy 151 (2015) 160–167, https://doi.org/10.1016/j.ultramic.2014.09.013.

[35] H. Yang, T.J. Pennycook, P.D. Nellist, Efficient phase contrast imaging in STEM using a pixelated detector. Part II: optimisation of imaging conditions, Ultramicroscopy 151 (2015) 232–239, https://doi.org/10.1016/j.ultramic.2014.10.013.

[36] A. Kovács, R. Schierholz, K. Tillmann, FEI Titan G2 80-200 CREWLEY, J. Large-Scale Res. Facil. 2 (2016) A43, https://doi.org/10.17815/jlsrf-2-68.

[37] C. Boothroyd, A. Kovács, K. Tillmann, FEI Titan G2 60-300 HOLO, J. Large-Scale Res. Facil. 2 (2016) A44, https://doi.org/10.17815/jlsrf-2-70.

[38] J.M. Cowley, Diffraction Physics, Elsevier, 1995.

[39] E.G.T. Bosch, I. Lazić, Analysis of depth-sectioning STEM for thick samples and 3D imaging, Ultramicroscopy 207 (2019) 112831, https://doi.org/10.1016/j.ultramic.2019.112831.

[40] J.W. Goodman, Introduction to Fourier optics, McGraw-Hill Inc., New York, 1996.

[41] G. Pozzi, M. Beleggia, T. Kasama, R.E. Dunin-Borkowski, Interferometric methods for mapping static electric and magnetic fields, C. R. Phys. 15 (2014) 126–139, https://doi.org/10.1016/j.crhy.2014.01.005.

[42] G. Matteucci, G.F. Missiroli, E. Nichelatti, A. Migliori, M. Vanzi, G. Pozzi, Electron holography of long-range electric and magnetic-fields, J. Appl. Phys. 69 (1991) 1835–1842, https://doi.org/10.1063/1.348970.

[43] G. Matteucci, G.F. Missiroli, M. Muccini, G. Pozzi, Electron holography in the study of the electrostatic fields - the case of charged microtips, Ultramicroscopy 45 (1992) 77–83, https://doi.org/10.1016/0304-3991(92)90039-M.

[44] G. Matteucci, G.F. Missiroli, G. Pozzi, Electron holography of long-range electrostatic fields, Adv. Imag. Elect. Phys. 99 (1997) 171–240, https://doi.org/10.1016/S1076-5670(08)70242-8.

[45] G. Matteucci, G.F. Missiroli, G. Pozzi, Electron holography of long-range electrostatic fields, Adv. Imag. Elect. Phys. 122 (2002) 173–249, https://doi.org/10.1016/S1076-5670(02)80053-2.

[46] A.H. Tavabi, V. Migunov, C. Dwyer, R.E. Dunin-Borkowski, G. Pozzi, Tunable caustic phenomena in electron wavefields, Ultramicroscopy 157 (2015) 57–64, https://doi.org/10.1016/j.ultramic.2015.04.003.

[47] G. Pozzi, V. Grillo, P.H. Lu, A.H. Tavabi, E. Karimi, R.E. Dunin-Borkowski, Design of electrostatic phase elements for sorting the orbital angular momentum of electrons, Ultramicroscopy 208 (2020) 112861, https://doi.org/10.1016/j.ultramic.2019.112861.

[48] J. Caron, Model-based Reconstruction of Magnetisation Distributions in Nanostructures from Electron Optical Phase images, Dissertation, RWTH Aachen University, 2017.

[49] F. Zheng, J. Caron, V. Migunov, M. Beleggia, G. Pozzi, R.E. Dunin-Borkowski, Measurement of charge density in nanoscale materials using off-axis electron holography, J. Electron Spectrosc. Relat. Phenom. (2019) 146881, https://doi.org/10.1016/j.elspec.2019.07.002.

[50] A. Tikhonov, V. Arsenin, Solutions of Ill-Posed Problems (Scripta Series in Mathematics), V.H. Winston & Sons, 1977.

[51] M. Beleggia, T. Kasama, R.E. Dunin-Borkowski, S. Hofmann, G. Pozzi, Direct measurement of the charge distribution along a biased carbon nanotube bundle using electron holography, Appl. Phys. Lett. 98 (2011) 243101, https://doi.org/10.1063/1.3598468.

[52] C. Gatel, A. Lubk, G. Pozzi, E. Snoeck, M. Hytch, Counting elementary charges on nanoparticles by electron holography, Phys. Rev. Lett. 111 (2013) 025501, https://doi.org/10.1103/PhysRevLett.111.025501.

[53] J.F. Dushimineza, J. Jo, R.E. Dunin-Borkowski, K. Müller-Caspary, Quantitative electric field mapping between electrically biased needles by scanning transmission electron microscopy and electron holography, Ultramicroscopy 253 (2023) 113808, https://doi.org/10.1016/j.ultramic.2023.113808.

[54] D. Van Dyck, Through object electron holography, J. Electron Microsc. 48 (1999) 33–34, https://doi.org/10.1093/oxfordjournals.jmicro.a023647.

[55] T. Tanigaki, Y. Inada, S. Aizawa, T. Suzuki, H.S. Park, T. Matsuda, A. Taniyama, D. Shindo, A. Tonomura, Split-illumination electron holography, Appl. Phys. Lett. 101 (2012) 043101, https://doi.org/10.1063/1.4737152.

[56] K. Harada, H. Kasai, Accumulated Reconstruction Method for Electron Holography, Microsc. Microanal. 20 (2014) 248–249, https://doi.org/10.1017/s1431927614002967.

[57] M. Beleggia, T. Kasama, D.J. Larson, T.F. Kelly, R.E. Dunin-Borkowski, G. Pozzi, Towards quantitative off-axis electron holographic mapping of the electric field around the tip of a sharp biased metallic needle, J. Appl. Phys. 116 (2014) 024305, https://doi.org/10.1063/1.4887448.

[58] V. Migunov, A. London, M. Farle, R.E. Dunin-Borkowski, Model-independent measurement of the charge density distribution along an Fe atom probe needle using off-axis electron holography without mean inner potential effects, J. Appl. Phys. 117 (2015) 134301, https://doi.org/10.1063/1.4916609.